



# Chemically induced compaction bands: Triggering conditions and band thickness

Ioannis Stefanou, Jean Sulem

## ► To cite this version:

Ioannis Stefanou, Jean Sulem. Chemically induced compaction bands: Triggering conditions and band thickness. *Journal of Geophysical Research : Solid Earth*, American Geophysical Union, 2014, in press. <10.1002/2013JB010342>. <hal-00923844>

**HAL Id: hal-00923844**

**<https://hal-enpc.archives-ouvertes.fr/hal-00923844>**

Submitted on 5 Jan 2014

**HAL** is a multi-disciplinary open access archive for the deposit and dissemination of scientific research documents, whether they are published or not. The documents may come from teaching and research institutions in France or abroad, or from public or private research centers.

L'archive ouverte pluridisciplinaire **HAL**, est destinée au dépôt et à la diffusion de documents scientifiques de niveau recherche, publiés ou non, émanant des établissements d'enseignement et de recherche français ou étrangers, des laboratoires publics ou privés.

1                                   **Chemically induced compaction bands:**  
2                                   **Triggering conditions and band thickness**

3                                   Ioannis Stefanou and Jean Sulem

4                                   Université Paris-Est, Laboratoire Navier, CNRS (UMR 8205), ENPC, IFSTTAR

5  
6                                   Corresponding author: I.Stefanou, Ecole Nationale des Ponts et Chaussées, 77455 Marne la  
7                                   Vallée, Cedex 2, France, (ioannis.stefanou@enpc.fr)

8  
9                                   **Key points**

- 10                                  -    Compaction band instabilities due to cataclasis and dissolution in rocks  
11                                  -    Strong chemo-poro-mechanical coupling, grain breakage and chemical softening  
12                                  -    Regions of instability, compaction band thickness and periodicity

13  
14                                  **Abstract**

15                                  During compaction band formation various mechanisms can be involved at different scales.  
16                                  Mechanical and chemical degradation of the solid skeleton and grain damage are important  
17                                  factors that may trigger instabilities in the form of compaction bands. Here we explore the  
18                                  conditions of compaction band formation in quartz- and carbonate-based geomaterials by  
19                                  considering the effect of chemical dissolution and grain breakage. As the stresses/deformations  
20                                  evolve, the grains of the material break leading to an increase of their specific surface.  
21                                  Consequently, their dissolution is accelerated and chemical softening is triggered. By accounting  
22                                  for (a) the mass diffusion of the system, (b) a macroscopic failure criterion with dissolution  
23                                  softening and (c) the reaction kinetics at the micro level, a model is proposed and the conditions  
24                                  for compaction instabilities are investigated. Distinguishing the micro-scale (grain level) from the  
25                                  macro-level (Representative Elementary Volume) and considering the heterogeneous  
26                                  microstructure of the REV it is possible to discuss the thickness and periodicity of compaction  
27                                  bands. Two case studies are investigated. The first one concerns a sandstone rock reservoir which  
28                                  is water flooded and the second one a carbonate rock in which CO<sub>2</sub> is injected for storage. It is  
29                                  shown that compaction band instabilities are possible in both cases. (200 words)

30  
31  
32  
33                                  **Index terms**

34                                  STRUCTURAL GEOLOGY: Mechanics, theory and modeling

1 NONLINEAR GEOPHYSICS: Bifurcations and attractors, Critical phenomena, Pattern  
2 formation

3 COMPUTATIONAL GEOPHYSICS: Modeling

4

5 **Keywords**

6 Compaction band instabilities, Strain localization, Chemo-poro-mechanical coupling, Grain  
7 breakage, Rocks, Reservoirs

8

9

## 10 **1. Introduction**

11 The presence of compaction bands in nature may provide useful information on various  
12 geological processes as it is an indication of the stress state history of a geological formation.  
13 Compaction bands are usually characterized by a significant reduction of the pore space, which in  
14 most of the cases is accompanied by an important reduction in permeability. Thus, compaction  
15 bands are also important in reservoir mechanics for oil production and CO<sub>2</sub> storage [*Olsson et al.*,  
16 2002; *Holcomb et al.*, 2007; *Rutqvist*, 2012]. Pore collapse, intergranular grain fracturing and  
17 sliding, Hertzian cracking at grain contacts, grain crushing, grain attrition, grain-matrix  
18 debonding and matrix fracturing are often observed to a less or bigger extent inside the  
19 compacting zone [*Baud et al.*, 2004, 2009; *Sternlof et al.*, 2005; *Tondi et al.*, 2006; *Holcomb et*  
20 *al.*, 2007; *Aydin and Ahmadov*, 2009; *Zhu et al.*, 2010; *Cilona et al.*, 2012; *Rustichelli et al.*,  
21 2012; *Wong and Baud*, 2012]. In parallel, it has been observed that reactive fluids play a  
22 significant role in creep and compaction of porous rocks [e.g. *Le Guen et al.*, 2007; *Liteanu and*  
23 *Spiers*, 2009; *Rutqvist*, 2012]. Generally, mechanical damage and chemical degradation of the  
24 solid skeleton (i.e. of the grains and matrix) are important factors that may trigger instabilities in  
25 the form of compaction bands. The objective of the present paper is to explore the possibilities  
26 and conditions of compaction band formation due to chemo-mechanical reasons in porous  
27 geomaterials.

28  
29 In the frame of Continuum Mechanics, compaction bands can be seen as an instability of the  
30 underlying mathematical problem. Discrete approaches like the Discrete Element Method have  
31 also been proposed in the literature [*Katsman et al.*, 2005; *Katsman and Aharonov*, 2006; *Wang*  
32 *et al.*, 2008; *Marketos and Bolton*, 2009, among others] but they are computationally intensive  
33 and the identification of the general conditions that lead to strain localization is not  
34 straightforward. On the other hand a continuum approach can reveal the conditions for  
35 compaction band triggering given the constitutive behavior of the material [*Rudnicki and Rice*,  
36 1975; *Vardoulakis and Sulem*, 1995; *Rudnicki*, 2002]. It is commonly observed that strain  
37 localization is favored by strain softening and most of the existing theoretical studies focus on  
38 pure mechanical reasons for compaction band formation (mechanical softening due to grain and  
39 matrix damage and pore collapse). Nevertheless, more recently, the role of chemical softening on

40 slip instabilities has been explored [e.g. *Brantut and Sulem, 2012; Veveakis et al., 2012, 2013*]  
41 showing that chemistry may play an important role in shear band instabilities and strain  
42 localization. Here we focus on the conditions that lead to the formation of pure compaction bands  
43 in quartz- or carbonate-based geomaterials by considering the effect of chemical dissolution.  
44 Shear enhanced compaction bands are out of the scope of the present study and their investigation  
45 can be a future extension of the proposed model.

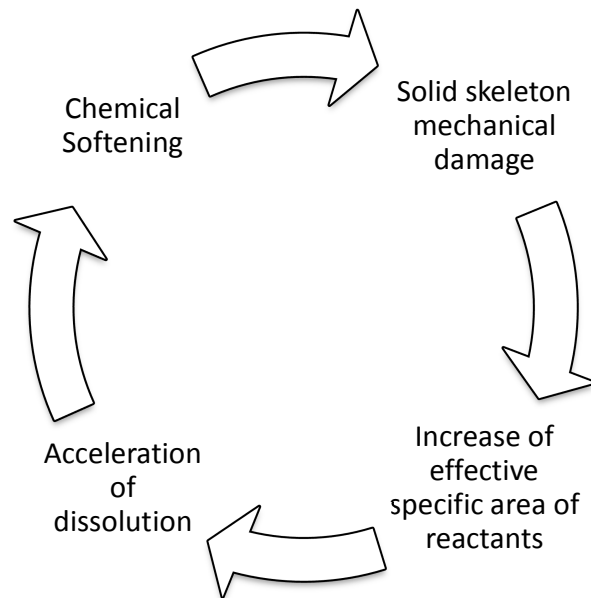
46  
47 The effect of chemical dissolution is important in field and in reservoir applications. For instance,  
48 the experimental results of Xie et al. [2011] showed that the chemical dissolution of a limestone  
49 leads to a significant increase of the porosity (from 23% for the intact rock to 27% for the  
50 degraded one). According to the same authors, the plastic pore collapse threshold is also reduced  
51 from about 30 to 20 MPa and the chemically degraded materials become more collapsible and  
52 more ductile due to the increase in porosity and the degradation of the inter-granular cementation.  
53 This evidence is corroborated by other authors [e.g. *Nova et al., 2003; Hu and Hueckel, 2007b;*  
54 *Zinsmeister et al., 2013*] for a class of geomaterials and results in a contraction of the elastic  
55 domain only due to chemical reasons (chemical softening). In parallel, in a saturated porous  
56 geomaterial, the progressive mechanical damage of the solid skeleton during compaction has as a  
57 result the increase of the interface area of the reactants (i.e. of the solution with the solid) and  
58 consequently the acceleration of the dissolution rate of the solid phase [cf. *Rimstidt and Barnes,*  
59 *1980*]. Thus, the solid skeleton is degraded more rapidly (mass removal because of dissolution),  
60 the overall mechanical properties of the system diminish (contraction of the elastic domain –  
61 chemical softening), deformations increase and the solid skeleton is further damaged  
62 (intergranular fractures, debonding, breakage of the porous network etc.). Figure 1 schematically  
63 shows this positive feedback process, whose stability is not guaranteed. Actually, as it will be  
64 shown in this paper, instabilities in the form of compaction bands may be triggered.

65  
66 The impact of chemical phenomena and, in particular, of pressure solution inside deformation  
67 bands, has been demonstrated in several cases [*Tondi et al., 2006; Tondi, 2007; Liteanu and*  
68 *Spiers, 2009; Cilona et al., 2012; Rustichelli et al., 2012*]. However, the effect of dissolution on  
69 compaction band formation is difficult to observe in the field and its exact role is still a subject of  
70 investigation. Notice that field observations are made long after the formation of compaction

71 bands, where the poro-mechanical properties of the rock have obviously drastically changed.  
72 Exploring the effects of dissolution prior to compaction band formation is also a difficult task in  
73 the laboratory as the reproduction of the field conditions is not straightforward. Nevertheless,  
74 recent experimental tests with dissolvable surrogate materials and numerical studies with the  
75 Discrete Element Method have shown that dissolution of grains causes pronounced changes in  
76 the fabric and in the intergranular force transmission that may result in episodic microstructural  
77 changes and to strain localization [*Shin, 2009; Shin and Santamarina, 2009; Tran et al., 2012*].  
78 The aforementioned indications of chemically induced strain localization instabilities provides  
79 the motivation of the present study and justifies the consideration of strong chemo-mechanical  
80 couplings in models due to dissolution.

81  
82 Two scales are distinguished in the present chemo-hydro-mechanical model. The first scale is  
83 related to the macroscopic poromechanical behavior of the geomaterial. At this level the mass  
84 balance equation and the stress equilibrium are expressed over the representative elementary  
85 volume (REV). The second scale, which will be called here micro-scale, concerns the behavior of  
86 a single grain of the geomaterial and its surrounding matrix. Intergranular and matrix fracturing,  
87 grain-matrix debonding and the dissolution reaction kinetics refer to this scale. The distinction of  
88 the micro- and the macro-scale is presented schematically in Figure 2. The bridging between the  
89 macro- and the micro-scale is achieved here through the empirical law of Lade [1996], which  
90 relates the effective grain size to the mechanical energy input to the system. In this sense, at least  
91 part of the mechanical energy is dissipated through the various micro-mechanisms related to the  
92 solid skeleton damage for the creation of new surfaces in the medium (fracturing). The advantage  
93 of the aforementioned empirical law over other micromechanical approaches is that it needs the  
94 calibration of only one parameter. More sophisticated grain damage models that account for the  
95 degradation of the inter-granular cement of rocks might be suitable, but the chosen  
96 phenomenological approach is a first step for studying some key features of chemical degradation  
97 on compaction banding by avoiding unnecessary complexity. Dissolution reaction kinetics at the  
98 micro-level (i.e. at the scale of a single grain) are then up-scaled to the macro-level.

99



100

101 *Figure 1. Positive feedback process due to dissolution and solid skeleton damage (e.g.*  
 102 *intergranular fracturing, breakage of the porous network, matrix cracking, grain-matrix*  
 103 *debonding etc.)*

104

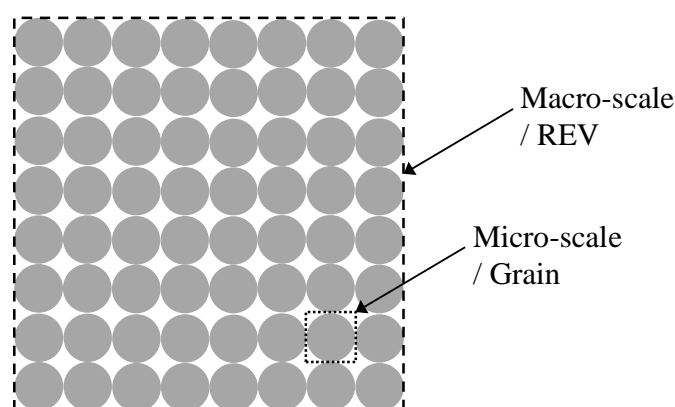
105 As it was already mentioned, the present analysis aims at exploring the possibilities of  
 106 compaction band formation due to chemical softening effects only. Therefore, mechanical  
 107 softening (or hardening) induced by grain damage or pore collapse is not considered herein in  
 108 order to isolate the chemical effects. This means that the effect of grain damage and pore collapse  
 109 on the evolution of the yield surface as described for instance by Das et al. [2011] is neglected.  
 110 On the other hand the effect of the damage of the solid skeleton on the acceleration of chemical  
 111 reaction is taken into account by explicitly introducing the effective specific surface of the grains  
 112 in the reaction kinetics law. Of course it is possible to account also for mechanical  
 113 softening/hardening due to grain damage and pore collapse but this would somewhat hide the role  
 114 of chemical effects explored here.

115

116 The first two sections of the paper are devoted to the formulation of the proposed chemo-pro-  
 117 mechanical model by distinguishing the micro- and the macro-level behavior. At the macro-level  
 118 (section 2), the constitutive behavior of the material is described within the frame of plasticity  
 119 theory, the mass balance equation is derived and the linear momentum balance is set forth in

120 order to account for the different species in the REV. At the micro-level (section 3), the evolution  
 121 of the effective grain size due to various micro mechanisms is described and the reaction kinetics  
 122 are formulated and upscaled to the macro-level. Next, in section 4, the possibility of compaction  
 123 band formation is discussed through a linear stability analysis. A criterion for compaction band  
 124 instabilities is proposed and its sensitivity to the various parameters of the model is explored.  
 125 Note that because of the strong chemo-poro-mechanical coupling, the application of the classical  
 126 localization criterion of Rice [1976] is not straightforward. Finally, in section 5 two examples of  
 127 compaction band instabilities are given for a quartzic rock under water flooding conditions and  
 128 for a carbonate grainstone in relation with CO<sub>2</sub> injection and storage. All the mathematical  
 129 calculations were performed with the symbolic language mathematical package Mathematica©  
 130 and they are available to the reader upon request.

131



132

133 *Figure 2. Schematic representation of the REV (macro-scale) and of the grains (micro-scale).*  
 134 *The picture is an idealization of the microstructure of a rock. The dissolution rate is*  
 135 *homogeneous in the REV when the size and the chemical composition of the grains is*  
 136 *homogeneous. In the case of compaction bands, the grains break, their size is not necessarily*  
 137 *uniform in the REV and consequently the dissolution rate is not any more homogeneous.*

138

## 139 **2. Macro-scale**

### 140 **2.1. Constitutive behavior**

141 Based on experimental research and theoretical considerations, several constitutive laws have  
 142 been proposed in the literature that relate the observed macroscopic stresses and strains. Plasticity



143 theory is a standard framework for the mathematical formulation of the underlying mechanical  
 144 problem. For a recent review of common plasticity models used for porous rocks we refer to  
 145 Wong and Baud [2012].

146  
 147 Depending on the applied stress path, the boundary conditions and the geomaterial at hand, a  
 148 strain hardening or softening response can be observed due to the various mechanisms, which  
 149 take place at the microlevel, i.e. at the grain-scale, and are related to the evolution of the  
 150 microstructure of the solid skeleton (e.g. pore collapse) and to grain damage (e.g. grain  
 151 fracturing). However, for the reasons exposed in the introduction, only chemical softening will be  
 152 considered herein.

153  
 154 The removal of minerals from the solid skeleton through chemical processes causes the  
 155 mechanical strength of the rock to decrease [e.g. *Hu and Hueckel, 2007a, 2007b*]. Therefore, we  
 156 expect the mechanical strength of a rock to be a function of the (residual) mass of the solid

157 skeleton after the dissolution process. Expressing as  $\zeta = \zeta(t) = \frac{M_s(t)}{M_s^0}$ ,  $0 \leq \zeta \leq 1$ , the ratio of the

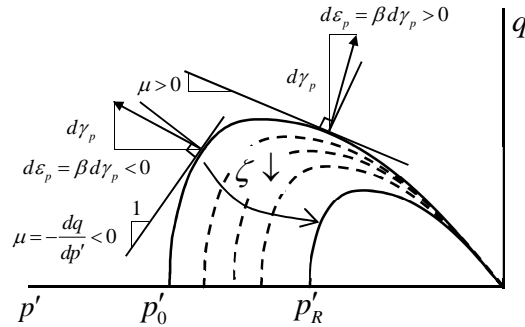
158 current mass,  $M_s(t)$ , of the constituent 's' over its initial mass,  $M_s^0 = M_s(t=0)$ , in the REV  
 159 before the chemical process starts (initial/reference state),  $\zeta$  can be seen as a chemical softening  
 160 parameter [see also Nova et al., 2003; Hu and Hueckel, 2007b]. Assuming compression negative,  
 161 Figure 3. describes qualitatively the strength domain of the geomaterial in the  $q - p'$  plane due  
 162 to chemical softening, i.e. for decreasing  $\zeta$ . The scalars  $p'$  and  $q$  are respectively the Terzaghi  
 163 effective mean stress (i.e. the difference between the total mean stress and the pore pressure) and  
 164 the shearing stress intensity. The shearing stress intensity  $q$  is defined as the square root of the

165 second invariant of the deviatoric part,  $s_{ij}$ , of the stress tensor:  $q = \sqrt{\frac{1}{2} s_{ij} s_{ji}}$ . The Einstein

166 summation convention is adopted. In order to preserve the generality of the approach we consider  
 167 a general yield surface of the form:

168 
$$f \equiv f(q, p', p'_c) = 0 \quad (1)$$

169 where  $p'_c$  is a material parameter (namely the yield stress under isotropic loading) which is  
 170 assumed to decrease from  $p'_0$  (initial reference state) to  $p'_R$  (residual yield stress once the  
 171 chemical reaction is completed) according to the following law  $p'_c \equiv p'_R - (p'_R - p'_0)\zeta^\kappa$  (Figure  
 172 3).  $\kappa$  is an exponent that can be experimentally determined for the material and the chemical  
 173 process at hand.



174  
 175 *Figure 3. Chemical isotropic softening due to dissolution of a constituent.  $\zeta$  describes the ratio*  
 176 *of the residual mass of the constituent in the REV over its initial (reference) mass before the*  
 177 *dissolution process. Compression is taken negative.  $\beta > 0$  corresponds to dilatancy and  $\beta < 0$  to*  
 178 *contractancy (decrease of porosity).*

179  
 180 In the frame of a small strain theory, the strain may be separated into elastic and plastic parts as  
 181 follows:

182 
$$\varepsilon = \varepsilon^e + \varepsilon^p \quad \text{and} \quad \gamma = \gamma^e + \gamma^p \quad (2)$$

183 where  $\varepsilon$  denotes the volumetric deformation and  $\gamma$  the shearing strain intensity  $\gamma = \sqrt{2e_{ij}e_{ji}}$

184 with  $e_{ij}$  being the deviatoric strain tensor.

185

186 The elasto-plastic incremental stress-strain relationships are given by:

187 
$$\dot{\boldsymbol{\sigma}}' = \mathbf{M}_{ep} \dot{\boldsymbol{\varepsilon}} + \boldsymbol{\Psi} \dot{\zeta} \quad (3)$$

188 where  $\boldsymbol{\sigma}' = \begin{pmatrix} p' \\ q \end{pmatrix}$ ,  $\boldsymbol{\varepsilon} = \begin{pmatrix} \varepsilon \\ \gamma \end{pmatrix}$ ,  $\mathbf{M}_{ep} = \left[ \mathbf{I} - \frac{\mathbf{M}_e \frac{\partial g}{\partial \boldsymbol{\sigma}} \left( \frac{\partial f}{\partial \boldsymbol{\sigma}} \right)^T}{\left( \frac{\partial f}{\partial \boldsymbol{\sigma}} \right)^T \mathbf{M}_e \frac{\partial g}{\partial \boldsymbol{\sigma}}} \right] \mathbf{M}_e$ ,  $\boldsymbol{\Psi} = -\frac{\mathbf{M}_e \frac{\partial f}{\partial \zeta} \frac{\partial g}{\partial \boldsymbol{\sigma}}}{\left( \frac{\partial f}{\partial \boldsymbol{\sigma}} \right)^T \mathbf{M}_e \frac{\partial g}{\partial \boldsymbol{\sigma}}}$ ,  $\mathbf{I}$  is the identity

189 matrix and  $\mathbf{M}_e = \begin{pmatrix} K & 0 \\ 0 & G \end{pmatrix}$  the elasticity matrix.  $(\cdot)^T$  denotes the transpose of  $(\cdot)$ .  $K$  and  $G$  are  
 190 respectively the elastic bulk and the elastic shear moduli of the geomaterial.  $g$  is the plastic  
 191 potential which can be identified to the yield surface,  $f$ , in case of associate plasticity. For a  
 192 general plastic constitutive law, we can write:

193 
$$\frac{\partial f}{\partial \boldsymbol{\sigma}} = \begin{pmatrix} \mu \\ 1 \end{pmatrix}, \quad \frac{\partial g}{\partial \boldsymbol{\sigma}} = \begin{pmatrix} \beta \\ 1 \end{pmatrix} \quad (4)$$

194 where  $\beta$  is the dilatancy angle ( $\beta > 0$  for dilatant materials) and  $\mu$  is the internal friction of the  
 195 geomaterial that depend on the actual state of stress. Using Eq.(4) we obtain:

196 
$$\mathbf{M}_{ep} = \frac{GK}{G + \beta\mu K} \begin{pmatrix} 1 & -\beta \\ -\mu & \beta\mu \end{pmatrix} \quad (5)$$

197 and

198 
$$\boldsymbol{\Psi} = \frac{1}{G + \beta\mu K} \begin{pmatrix} \beta K \\ G \end{pmatrix} \frac{\partial f}{\partial \zeta} \quad (6)$$

199 with

200 
$$\frac{\partial f}{\partial \zeta} = \frac{\partial f}{\partial p'_c} \frac{dp'_c}{d\zeta} = \frac{\partial f}{\partial p'_c} \kappa (p'_R - p'_0) \zeta^{\kappa-1} \quad (7)$$

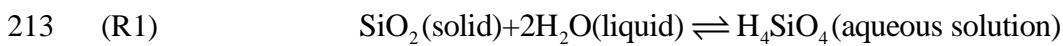
201 It is worth mentioning, that under constant loading, chemical softening would result in the  
 202 gradual accumulation of plastic deformations, which are controlled by the dissolution reaction  
 203 kinetics. This accumulation of deformations under constant loading can be seen as a creep

204 behavior induced by the chemical process of dissolution. Creep phenomena due to reactive fluids  
 205 injection are observed in laboratory tests on porous rocks [*Le Guen et al.*, 2007; *Liteanu and*  
 206 *Spiers*, 2009; *Shin and Santamarina*, 2009; *Brantut et al.*, 2013; *Croizet et al.*, 2013].

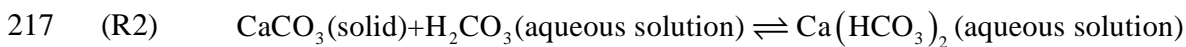
207

## 208 **2.2. Mass balance**

209 The dissolution of minerals is described by appropriate chemical reactions. According to the  
 210 reaction's stoichiometry the minerals of a rock may be degraded and transformed to amorphous  
 211 solid or liquid. For example the dissolution/precipitation of quartz in water is described by the  
 212 following chemical equation:



214 At equilibrium the silicic acid ( $\text{H}_4\text{SiO}_4$ ) is dissolved in the water with a concentration of the  
 215 order of few ppm. Another example is the dissolution of calcite with water that is saturated with  
 216 carbon dioxide:



218 This equation represents a set of consecutive reactions that take place and are responsible for the  
 219 dissolution of carbonate rocks [*Grgic*, 2011].

220 Here we consider any dissolution process of the form:



222 The reaction kinetics of this general equation will be analyzed in the next section.

223

224 At the macro-scale, the REV can be seen as a porous medium. The mass of the solid phase is  $M_3$   
 225 (e.g.  $\text{SiO}_2$ ) and the mass of the fluid phase is  $M_f = M_1 + M_2$ , where  $M_1$  is the mass of the  
 226 solvent (e.g.  $\text{H}_2\text{O}$ ) and  $M_2$  the mass of the dissolution product (e.g.  $\text{H}_4\text{SiO}_4$ ).

227 Following the notation of Coussy [2004] the mass balance equations hold:

228 
$$\frac{d^f M_1}{dt} = \frac{d}{dt}(\rho_{f1} n_1 d\Omega_t) = \dot{r}_{1 \rightarrow 2} d\Omega_t \quad (8)$$

229 
$$\frac{d^f M_2}{dt} = \frac{d}{dt}(\rho_{f2} n_2 d\Omega_t) = (\dot{r}_{2 \rightarrow 1} + \dot{r}_{2 \rightarrow 3}) d\Omega_t \quad (9)$$

230 
$$\frac{d^s M_3}{dt} = \frac{d}{dt}[\rho_s (1-n) d\Omega_t] = \dot{r}_{3 \rightarrow 2} d\Omega_t \quad (10)$$

231 where  $\frac{d^\chi}{dt}$  is the particle derivative,  $\rho_\chi$  is the density and  $n_\chi$  is the Eulerian porosity referring to  
 232 particle  $\chi$  ( $f$  for fluid and  $s$  for solid species),  $\dot{r}_{\chi \rightarrow \psi}$  represents the rate of mass of  $\chi$   
 233 transformed to  $\psi$  and  $d\Omega_t$  is the material volume in the current configuration. By definition:

234 
$$\rho_{f1} n_1 + \rho_{f2} n_2 = \rho_f n \quad (11)$$

235 where  $\rho_f$  is the density of the solution, which depends on the reactant's concentrations, the  
 236 pressure  $p_f$  and the temperature. Equations (8) and (9) lead to:

237 
$$\frac{d^f}{dt}(\rho_f n d\Omega_t) = \dot{r}_{2 \rightarrow 3} d\Omega_t \quad (12)$$

238 Considering isothermal conditions and constant density for the solid phase, Eqs.(10) and (12)  
 239 become:

240 
$$-\frac{\partial n}{\partial t} + \nabla_{\mathbf{x}} \mathbf{V}_s - \nabla_{\mathbf{x}}(n \mathbf{V}_s) = -\frac{1}{\rho_s} \dot{r}_{2 \rightarrow 3} \quad (13)$$

241 
$$\frac{\partial n}{\partial t} + n \frac{1}{\rho_f} \frac{\partial \rho_f}{\partial p_f} \frac{\partial p_f}{\partial t} + n \frac{1}{\rho_f} \frac{\partial \rho_f}{\partial w_2} \frac{\partial w_2^M}{\partial t} + \frac{1}{\rho_f} \nabla_{\mathbf{x}}(\rho_f) n \mathbf{V}_f + \nabla_{\mathbf{x}}(n \mathbf{V}_f) = \frac{1}{\rho_f} \dot{r}_{2 \rightarrow 3} \quad (14)$$

242 where the Nabla operator refers to the initial configuration ( $\mathbf{X}$  is the position vector of the solid  
 243 particles in the initial configuration),  $\mathbf{V}_s$  and  $\mathbf{V}_f$  are respectively the velocities of the solid phase

244 and fluid particles,  $p_f$  the fluid pressure and  $w_2^M = \frac{M_2}{M_f}$  the average dissolution product to fluid  
 245 mass fraction over the REV (macro-scale). Adding Eqs. (13) and (14) and using the chain rule,  
 246 the pore pressure diffusion-generation equation is obtained:

$$247 \quad \frac{\partial p_f}{\partial t} = c_{hy} \nabla_{\mathbf{x}}^2 p_f - \frac{1}{\beta^*} \frac{\partial \varepsilon}{\partial t} - c_{p,ch} \frac{\partial w_2}{\partial t} \quad (15)$$

248 where  $c_{hy}$  is the hydraulic diffusivity and  $\beta^* = n\beta_f$  with  $\beta_f = \frac{1}{\rho_f} \frac{\partial \rho_f}{\partial p_f}$  is the compressibility of  
 249 the fluid [see also *Ghabezloo and Sulem, 2008*]. For plastic incompressibility of the solid phase  
 250 and of the fluid,  $\beta^* = \frac{1}{K}$ . For the derivation of the pore pressure diffusion-generation equation,  
 251 the Darcy law was assumed and the gradient of the density of the fluid was ignored as being  
 252 negligible compared to the other terms of the equation. The deformation of the solid skeleton, i.e.  
 253 the term  $\nabla_{\mathbf{x}} \mathbf{V}_s = \frac{\partial \varepsilon}{\partial t}$ , is responsible for the hydro-mechanical coupling. In the right hand side of  
 254 the equation the last term expresses the pore pressure change due to dissolution/precipitation  
 255 process and  $c_{p,ch}$  is the chemical pressurization coefficient, which depends on the evolution of  
 256 the fluid density because of the reaction process. Herein, we neglect this effect as it does not  
 257 affect the stability of the system and generally its influence is limited [*Stefanou and Sulem,*  
 258 *2013*]. Finally, for small strains  $\nabla_{\mathbf{x}} \approx \nabla_{\mathbf{x}}$ , where  $\mathbf{x}$  is the position vector of the solid particles in  
 259 the current configuration.

260

### 261 **2.3. Momentum balance under oedometric conditions**

262 Under oedometric conditions the stress equilibrium is expressed as follows:

$$263 \quad \sigma_{zz,z} = 0 \quad (16)$$

264 where  $\sigma_{ij} = \sigma'_{ij} - p_f \delta_{ij}$ ,  $\delta_{ij}$  is the Kronecker delta,  $\sigma_{zz} = p - \frac{2}{\sqrt{3}} q$ ,  $\gamma = -\frac{2}{\sqrt{3}} \varepsilon_{zz}$ ,  $\varepsilon = \varepsilon_{zz}$ ,

265  $\varepsilon_{zz} = u_{z,z}$   $\varepsilon_{rr} = \varepsilon_{\theta\theta} = 0$  (for axisymmetric conditions). Using Eq.(3) we obtain:

266 
$$\dot{\sigma}'_{zz} = c \left( \Lambda \dot{\epsilon}_{zz} + \frac{\partial f}{\partial \zeta} \dot{\zeta} \right) \quad (17)$$

267 where  $\Lambda = K \frac{\left(1 + \frac{2}{\sqrt{3}}\beta\right)\left(1 + \frac{2}{\sqrt{3}}\mu\right)}{\frac{2}{\sqrt{3}} - \beta\frac{K}{G}}$  and  $c = \frac{\frac{2}{\sqrt{3}} - \beta\frac{K}{G}}{1 + \beta\mu\frac{K}{G}}$ .  $c\Lambda$  expresses the change of the

268 effective vertical stress due to compaction and  $c\frac{\partial f}{\partial \zeta}$  its change due to chemical degradation.

### 269 3. Micro-scale

#### 270 3.1. Cataclasis, solid skeleton damage and evolution of the effective grain size

271 A rock can be seen as an assemblage of bonded grains, which during deformation may break into  
 272 smaller grains with rupture of bonds. Following Lade et al. [1996] the grain size reduction is  
 273 related to the total energy input. In this sense, at least part of the mechanical energy is dissipated  
 274 through various micro-mechanisms for the creation of new surfaces in the medium (grain  
 275 fracturing). “Hertzian cracks” at the grain contacts (intergranular fracturing, grain crushing, grain  
 276 attrition etc.), “microcracking” of the cementitious matrix [Aydin and Ahmadov, 2009; Cilona et  
 277 al., 2012] and grain debonding [Castellanza and Nova, 2004] are some important mechanisms  
 278 that lead to the reduction of the effective grain size of the geomaterial and consequently to the  
 279 increase of the dissolution front.

280

281 Under this framework, it is convenient to define an effective grain size,  $D$ , whose evolution  
 282 reflects the effect of grain damage. According to Lade et al. [1996], for a given grain size  
 283 distribution, this effective grain size is commonly taken equal to  $D_{10}$  (10% of the system weight  
 284 consists of grains below  $D_{10}$  diameter). Generally, the choice of the appropriate effective grain  
 285 size depends on the exact grain size distribution and the material at hand. For instance in the case  
 286 of shear bands created in the laboratory  $D_{10}$  seems a good measure for the effective grain size  
 287 reduction [El Bied et al., 2002]. On the other hand, in the case of compaction bands observed in  
 288 the field,  $D_{50}$  seems a better choice [Cilona et al., 2012].

289

290 Lade et al. [1996] proposed the following expression for the evolution of grain crushing of a  
 291 granular material in terms of the mechanical work input:

$$292 \quad D = D_0 \left( \frac{a}{a + E_T} \right) \quad (18)$$

293 where  $D_0$  is the effective grain size of the initial gradation and  $E_T$  is the total energy input per  
 294 specimen unit volume (including the energy due to isotropic compression and shearing).  $a$  is a  
 295 fitting parameter, which will be called here grain damage sensitivity parameter that expresses the  
 296 extent of the grain size change due to energy input. For large values of parameter  $a$ , as compared  
 297 to  $E_T$ , the grain size is constant. As discussed by Lade et al. [1996], the total energy seems to be a  
 298 more relevant parameter for describing grain breakage compared to the effective mean stress or  
 299 the void ratio. As an example, for Cambria sand  $a = 0.747\text{MPa}$  [Lade et al., 1996]. For a rock,  
 300 the parameter  $a$  should also depend on the grain size distribution [cf. Cheung et al., 2012].  
 301 Considering that the specific effective surface of a grain  $S$  (effective grain surface area to  
 302 volume ratio) is inversely proportional to the grain diameter, it is natural to assume the same type  
 303 of relationship:

$$304 \quad S = S_0 \left( 1 + \frac{E_T}{a} \right) \quad (19)$$

305 It is worth emphasizing that the grains of rocks are often cemented together and that the  
 306 consideration of the rock as a granular material, with well-defined grain to pore fluid interactions  
 307 is rather an idealization of reality. Nevertheless, as it was mentioned above, the dissipation during  
 308 mechanical loading is mainly attributed to internal friction mechanisms (reorganization of grains,  
 309 grain dislocation/disclination) and microcracking of both the grains and of the cementitious  
 310 matrix (Hertzian cracking, microcracking, debonding etc.). In this sense, Eq.(19), could also be  
 311 used in order to describe the increase of the specific surface of the grains of a cemented granular  
 312 material like a porous rock. Parameter  $a$  may be calibrated either through appropriate  
 313 micromechanical models that take into account the micro-cracking of the matrix and grain  
 314 breakage [e.g. Das et al., 2011] or through adequate experimental tests. More specifically, the  
 315 value of the grain damage parameter may be determined experimentally through acoustic



316 emissions, X-ray tomography or other experimental techniques [Wong and Baud, 2012] that will  
 317 correlate the effective grain size due to grain damage and the mechanical energy input.

318  
 319 Finally, it should be mentioned that grain crushing results in a reduction of porosity and generally  
 320 to a reduction of permeability [Walsh and Brace, 1984; Sulem and Ouffroukh, 2006]. Moreover,  
 321 due to dissolution, the specific area of the grains at the microscale is increased and the existing  
 322 microcracks propagate further (subcritical growth, stress corrosion cracking). Therefore, the grain  
 323 crushing sensitivity parameter,  $a$ , is not necessarily constant in time and may depend on the  
 324 reaction kinetics, the stress level and the nature of the saturating fluid. However, in the linear  
 325 stability analysis presented in the next section, the permeability change due to porosity reduction  
 326 is of second order and can be neglected for the onset of strain localization. Nevertheless, for  
 327 performing numerical simulations of rocks with the proposed chemo-poro-mechanical model it is  
 328 possible to determine the evolution of these parameters based on empirical and/or theoretical  
 329 models.

330

### 331 **3.2. Reaction kinetics**

332 According to Rimstidt and Barnes [1980] the rate of reaction between the fluid and solid phase  
 333 during quartz dissolution (or precipitation, R1) is directly proportional to the interfacial area  
 334 between the solid and the liquid phase. The dissolution rate is commonly assumed to be  
 335 proportional to the mineral surface area exposed to the aqueous solution [Cubillas *et al.*, 2005].  
 336 Here we generalize this idea for any dissolution process of the form of R3. The rate of production  
 337 (or consumption) of moles of the dissolution product is considered to obey the following rate  
 338 equation:

$$339 \quad \frac{\partial n_2}{\partial t} = Ak(1 - \Omega) \quad (20)$$

340 where  $n_2$  is the number of moles of the product of the dissolution process (e.g. the  $\text{H}_4\text{SiO}_4$  or the  
 341  $\text{Ca}(\text{HCO}_3)_2$ ),  $A$  the available interfacial area of the solid with the solution,  $k$  the dissolution  
 342 rate constant per unit area of the interface and  $\Omega$  is the degree of saturation. If  $\Omega = 1$  the reaction

343 is at equilibrium, if  $\Omega < 1$  dissolution takes place and if  $\Omega > 1$  precipitation happens.  $\Omega$  is  
 344 expressed in terms of the reaction quotient,  $Q$ , and the equilibrium constant,  $K_{eq}$ , as follows:

$$345 \quad \Omega = \frac{Q}{K_{eq}} \quad (21)$$

346 It is worth mentioning that in order to account for the intergranular dissolution-diffusion micro-  
 347 mechanisms that take place in the thin aqueous film that is developed at the grain contacts, a  
 348 chemical potential that depends on the stress state is often considered (pressure solution [Rutter,  
 349 1983]). As a result, the reaction kinetics (i.e. Eq. (20), equilibrium constant, reaction rate) might  
 350 be functions of the stress state. However, intense cataclasis (stress induced cracking, grain  
 351 breakage, microcracking, debonding etc.) is often observed inside the zone of deformation bands  
 352 [Baud *et al.*, 2009; Cilona *et al.*, 2012]. Therefore, in the stability analysis performed in the next  
 353 section, the reaction kinetics will not directly depend on the stress state, but will be a function of  
 354 the available interaction surface of the reactants (dissolution of grains), which depends on the  
 355 stress state because of grain damage.

356  
 357 Assuming that the reaction activity coefficients for the reactants are close to unity and that  
 358  $w_2 \ll 1$ , Eq.(20) and (21) give (Appendix A.1):

$$359 \quad \frac{\partial w_2}{\partial t} = k^* \frac{S}{e} \left( 1 - \frac{w_2}{w_2^{eq}} \right) \quad (22)$$

360 where  $k^* = \frac{\mu_2}{\rho_f} k$ ,  $e = \frac{n}{1-n}$  is the void ratio and  $w_2^{eq}$  the mass fraction of dissolution product to  
 361 the fluid mass at chemical equilibrium. It should be emphasized that Eq.(22) is written at the  
 362 microscale and that  $w_2$ ,  $S$  and  $e$  represent local quantities, which are not necessarily  
 363 homogeneous over the REV (Figure 2). On the other hand, the constitutive law and the mass  
 364 balance represent quantities defined over the REV and therefore the aforementioned local  
 365 quantities have to be upscaled from the micro- to the macro-level.

366

367 **3.3. Chemical softening and upscaling**

368 At the macroscale the rate of the chemical softening parameter  $\zeta$  holds for  $w_2 \ll 1$  (Appendix  
369 A.2):

$$370 \quad \frac{\partial \zeta}{\partial t} = -\frac{\mu_3 \rho_f}{\mu_2 \rho_s} e^\zeta \frac{\partial w_2^M}{\partial t} \quad (23)$$

371 The average mass fraction of the dissolution product over the REV (macro-level) is related to the  
372 local mass fraction  $w_2$  (Figure 2) as follows:

$$373 \quad w_2^M = \frac{1}{V_T} \int_{V_T} w_2 dV \quad (24)$$

374 Assuming that  $w_2 = w_2(z, t)$  (oedometric conditions) is a function that can be expanded into  
375 Taylor series up to the second order in  $z$  :

$$376 \quad w_2(z_l, t) \approx w_2(z, t) + z_l \left. \frac{\partial w_2(z, t)}{\partial z} \right|_z + \frac{1}{2} z_l^2 \left. \frac{\partial^2 w_2(z, t)}{\partial z^2} \right|_z \quad (25)$$

377 where  $z_l$  is the coordinate in a local coordinate system with origins at the center of the REV,  $z$ ,  
378 injecting equation (25) to equation (24) and integrating over the REV we obtain:

$$379 \quad w_2^M \approx w_2 + \ell_c^2 \frac{\partial^2 w_2}{\partial z^2} \quad (26)$$

380 where  $\ell_c = \ell_{REV} \sqrt{\frac{1}{24}} \approx \frac{\ell_{REV}}{5}$  appears as a characteristic internal length and  $\ell_{REV}$  is the size of the  
381 REV in the  $z$  direction. Note that if the mass fraction is homogeneous all over the REV, then  
382  $w_2^M = w_2$ .

383 **4. Compaction band formation**

384 Equations (15), (16) and (22) describe the evolution of the system under oedometric conditions,  
385 while equation (26) links the macro- and micro-scale. Introducing the dimensionless quantities:

$$\begin{aligned}
\hat{w}_2^{(M)} &= \frac{w_2^{(M)}}{K_{eq}}, \quad \hat{p}_f = \frac{p_f}{\sigma_n}, \quad \hat{\sigma}_{ij} = \frac{\sigma_{ij}}{\sigma_n}, \quad \hat{p} = \frac{p}{\sigma_n}, \quad \hat{q} = \frac{q}{\sigma_n}, \quad \hat{E}_T = \frac{E_T}{\sigma_n}, \quad \hat{a} = \frac{a}{\sigma_n}, \quad \hat{\beta}^* = \beta^* \sigma_n \\
\hat{u}_i &= \frac{u_i}{D_0^{50}}, \quad \hat{L} = \frac{L}{D_0^{50}}, \quad \hat{S} = S D_0^{50}, \quad \hat{\rho}_\chi = \frac{\rho_\chi}{\rho_{H_2O}}, \quad \hat{t} = \frac{t}{T}, \quad \hat{c}_{hy} = \frac{T}{(D_0^{50})^2} c_{hy}
\end{aligned}
\tag{27}$$

with  $D_0^{50}$  the median grain diameter in the reference/initial state and choosing  $T = \frac{K_2^{eq} D_0^{50}}{k^*}$  as characteristic time, the aforementioned equations become:

$$\hat{\sigma}_{zz,\hat{z}} = 0 \tag{28}$$

$$\frac{\partial \hat{p}_f}{\partial \hat{t}} = \hat{c}_{hy} \frac{\partial^2 \hat{p}_f}{\partial \hat{z}^2} - \frac{1}{\hat{\beta}^*} \frac{\partial \varepsilon}{\partial \hat{t}} - \hat{c}_{p, ch} \frac{\partial \hat{w}_2^M}{\partial \hat{t}} \tag{29}$$

$$\frac{\partial \hat{w}_2}{\partial \hat{t}} = e^{-1} \hat{S} (1 - \hat{w}_2) \tag{30}$$

$$\hat{w}_2^M \approx \hat{w}_2 + \hat{\ell}_c^2 \frac{\partial^2 \hat{w}_2}{\partial \hat{z}^2} \tag{31}$$

In the following the hats over the variables will be dropped in order to simplify the notations.

It has to be mentioned that the application of the well-known localization (bifurcation) criterion of Issen & Rudnicki [Rudnicki and Rice, 1975; see also Rice, 1976; Bigoni and Hueckel, 1991; Issen and Rudnicki, 2000] is not straightforward in the present case where a chemo-poro-mechanical coupling takes place. For this reason a linear stability analysis is performed in the next section.

#### 4.1. Linear stability analysis

Let  $u_z^h$ ,  $p_f^h$  and  $w_2^h$  be the solutions of the above equations that lead to homogeneous deformation in space and  $\tilde{u}_z(z, t)$ ,  $\tilde{p}_f(z, t)$  and  $\tilde{w}_2(z, t)$  perturbations such that:

405

$$\begin{aligned}
u_z(z,t) &= u_z^h + \tilde{u}_z(z,t) \\
p_f(z,t) &= p_f^h + \tilde{p}_f(z,t) \\
w_2(z,t) &= w_2^h + \tilde{w}_2(z,t)
\end{aligned}
\tag{32}$$

406 The spatial dependence of the perturbations is decomposed into Fourier modes with wavelength  
407  $\lambda$  . Assuming zero fluid flux and no reaction evolution at the boundaries of the model:

408

$$\tilde{u}_z(z,t) = Ue^{st} \sin\left(\frac{z}{\ell}\right), \quad \tilde{p}_f(z,t) = Pe^{st} \cos\left(\frac{z}{\ell}\right) \quad \text{and} \quad \tilde{w}_2(z,t) = We^{st} \cos\left(\frac{z}{\ell}\right)
\tag{33}$$

409 where  $\lambda = 2\pi\ell = L/N$ ,  $N$  is equal to an integer satisfying the zero fluid flux and reaction  
410 evolution at the boundary  $z = \pm L/2$ , and  $s$  is the growth coefficient of the perturbation  
411 (Lyapunov exponent).  $s > 0$  means local instability.

412  
413 Introducing the above perturbations to Eqs.(28)-(30) and neglecting the higher order terms we  
414 obtain the system:

415

$$\tilde{\sigma}_{zz,z} = 0
\tag{34}$$

416

$$\frac{\partial \tilde{p}_f}{\partial t} = c_{hy} \frac{\partial^2 \tilde{p}_f}{\partial z^2} - \frac{1}{\beta^*} \frac{\partial \tilde{\varepsilon}}{\partial t}
\tag{35}$$

417

$$\frac{\partial \tilde{w}_2}{\partial t} = \frac{1-w_2^h}{e^h} \tilde{S} - \frac{S^h}{e^h} \left[ 1 + \eta^h (1-w_2^h) \right] \tilde{w}_2
\tag{36}$$

418

$$\tilde{w}_2^M \approx \tilde{w}_2 + \ell_c^2 \frac{\partial^2 \tilde{w}_2}{\partial z^2}
\tag{37}$$

419 where  $\eta^h = \frac{\mu_3}{\mu_2} \left( 1 + e^h \frac{\rho_f}{\rho_s} \right)$ . The superscript 'h' denotes the homogeneous state of the system.  $\tilde{S}$   
420 represents the perturbation of the specific surface because of the perturbations introduced in  
421 Eq.(32) and because of Eq.(19). All the above quantities are dimensionless (the hats were  
422 dropped for simplicity).

423

424 Substituting Eqs.(33) in the above equations, we obtain the following system of equations in  
425 matrix form:

$$426 \quad \mathbf{A} \cdot \mathbf{X} = \mathbf{0} \quad (38)$$

$$427 \quad \text{where } \mathbf{A} = \begin{pmatrix} \frac{A_{11}}{\ell^2} & -\frac{1}{\ell} & \frac{A_{13}}{\ell} \left(1 - \frac{\ell_c^2}{\ell^2}\right) \\ -\frac{s}{\ell} \frac{1}{\beta^*} & s + \frac{c_{hy}}{\ell^2} & 0 \\ -\frac{A_{32} S^h}{\ell} & 0 & s + S^h \varphi \end{pmatrix},$$

$$428 \quad A_{11} = -K \frac{\left(\frac{2\beta}{\sqrt{3}} + 1\right) \left(\frac{2\mu}{\sqrt{3}} + 1\right)}{1 + \frac{K}{G} \beta \mu}, \quad A_{13} = -\frac{\left(\frac{2}{\sqrt{3}} - \frac{K}{G} \beta\right)}{1 + \frac{K}{G} \beta \mu} \frac{\partial f}{\partial \zeta} \zeta^h e^h \frac{\rho_f \mu_3}{\rho_s \mu_2}, \quad A_{32} = \frac{1 - w^h}{ae^h},$$

$$429 \quad \varphi = \frac{1}{e^h} [1 + \eta^h (1 - w^h)] \quad \text{and} \quad \mathbf{X} = \begin{pmatrix} U \\ P \\ W \end{pmatrix}.$$

430

431 The system has non trivial solutions when the determinant of  $\mathbf{A}$  is zero, i.e.  $Det[\mathbf{A}] = 0$ , or  
432 equivalently:

$$433 \quad s^2 + C_1 s + C_0 = 0 \quad (39)$$

$$434 \quad \text{with } C_0 = \frac{S^h \beta^* c_{hy}}{\ell^2} \frac{\varphi A_{11} + A_{13} A_{32} \left(1 - \frac{\ell_c^2}{\ell^2}\right)}{A_{11} \beta^* - 1} \quad \text{and}$$

$$435 \quad C_1 = S^h \varphi + \frac{A_{11} c_{hy}}{A_{11} \beta^* - 1} \frac{1}{\ell^2} + S^h \frac{A_{13} A_{32}}{A_{11} \beta^* - 1} \left(1 - \frac{\ell_c^2}{\ell^2}\right).$$

436

437 If the real part of a root of the above quadratic equation (characteristic polynomial) is positive  
438 then the system is unstable.

439

440 **4.2. Conditions for instability**441 The roots  $s_1$  and  $s_2$  of the above quadratic equation satisfy:

442 
$$s_1 s_2 = C_0 \text{ and } s_1 + s_2 = -C_1 \quad (40)$$

443 Therefore if  $C_0 < 0$  then at least one root with positive real part exists. For  $A_{11} < 0$  and  $w^s < 1$ 444 (start of the reaction),  $C_0 < 0$  gives:

445 
$$\varphi A_{11} + A_{13} A_{32} \left( 1 - \frac{\ell_c^2}{\ell^2} \right) > 0 \quad (41)$$

446 or

447 
$$\frac{\partial f}{\partial \zeta} \zeta^h \left( 1 - \frac{\ell_c^2}{\ell^2} \right) < C_{cr} \quad (42)$$

448 where  $C_{cr} = -\frac{\Lambda \rho_s \mu_2}{\Xi \rho_f \mu_3}$  and  $\Xi = \frac{1 - w^h}{\varphi a}$ . This expression accounts for chemical softening due to449 dissolution and includes the characteristic length of the REV. When dissolution occurs,  $w^h < 1$ 450 and  $\Xi > 0$ . Moreover, in compression,  $d\varepsilon_{zz}^p = d\varepsilon^p < 0$  and therefore  $\beta < 0$ . Consequently,  $\Lambda$  is451 positive and  $C_{cr}$  is negative.  $\Lambda$  expresses the increase of the effective compressive stress452 because of compaction (see Eq.(17)).  $\frac{\partial f(\zeta)}{\partial \zeta} < 0$  expresses the contraction of the elastic domain453 (chemical softening) because of dissolution.  $\Xi$  represents the effect of dissolution on the stability454 of the system due to grain damage. The bigger the value of  $\Xi$  is (i.e., high effect of dissolution

455 due to grain damage) the more unstable the system becomes, as the instability condition (42) is

456 satisfied for a larger spectrum of  $\mu$  and  $\beta$  values (the instability region in the  $q-p$  plane is457 larger). The role of  $\Xi$  will be explored in the next paragraph458 In the special case where  $C_{cr} = 0$  ( $\mu = -\frac{\sqrt{3}}{2}$  or  $\beta = -\frac{\sqrt{3}}{2}$  leading to  $\Lambda = 0$ ), Eq. (42) becomes:

459 
$$\frac{\partial f}{\partial \zeta} \left( 1 - \frac{\ell_c^2}{\ell^2} \right) < 0 \quad (43)$$

460 and the system is unstable if  $\ell > \ell_c$ . In other words, the instability travels in space with a finite  
 461 wavelength ( $\lambda > 2\pi\ell_c \approx 1.2\ell_{REV}$ ) resulting in a compaction band of finite thickness. This will be  
 462 further investigated in the next paragraphs. Notice that in the absence of mechanical softening  
 463 and internal length ( $\ell_c = 0$ ) the above condition for compaction band instabilities ( $\mu = -\frac{\sqrt{3}}{2}$  or  
 464  $\beta = -\frac{\sqrt{3}}{2}$ ) coincides with the condition derived by Issen & Rudnicki [2000].

465  
 466 Finally, the above sufficient condition for instability should be completed with the following  
 467 condition in order to avoid the consideration of flutter instabilities, which are characterized by the  
 468 fact that the roots of the characteristic polynomial have an imaginary part:

469 
$$C_1^2 - 4C_0 \geq 0 \quad (44)$$

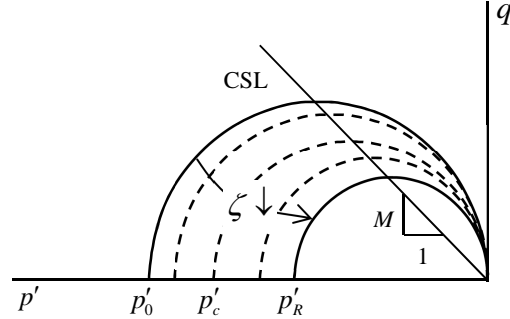
470 The reason for excluding this kind of oscillatory instabilities (blowing-up oscillations) is that they  
 471 seem unphysical for the chemo-mechanical problem at hand.

472  
 473 **4.3. Regions of stability and parameters sensitivity**

474 As an example of a cap yield surface we consider a modified Cam-clay yield surface with an  
 475 associate flow rule. Certainly, modified Cam-clay with associate flow rule is not the best  
 476 constitutive model for rocks and in order to obtain quantitative results an extensive experimental  
 477 research has to be conducted. Nevertheless, it is expected, that a general cap model, (Figure 3)  
 478 will be overall appropriate [Baud *et al.*, 2006; Wong and Baud, 2012]. Herein, we choose the  
 479 modified Cam-clay plasticity model with associate flow rule due to its relatively simple form (i.e.  
 480 elliptic yield cap). In particular the adopted yield surface is (Figure 4):



481 
$$f \equiv q^2 + M^2 p'(p' - p'_c) = 0 \quad (45)$$



483 *Figure 4. Modified Cam-clay model with chemical softening. Compression negative. CSL stands*  
 484 *for the critical state line, which is assumed constant.*

485 In this way the qualitative behavior of the system may be studied pointing out the effects of  
 486 chemical softening to compaction band formation. For the example at hand we consider the  
 487 following dimensionless parameters:  $p'_0 = -1$ ,  $p'_R = -0.2$ ,  $p_f = 0.4$ ,  $M = 1$ ,  $\kappa = 1$ ,  $K = G = 100$

488 ,  $S = 1$ ,  $c_{hy} = 6 \times 10^7$ ,  $\frac{\mu_3}{\mu_2} = 0.6$ ,  $\frac{\rho_f}{\rho_s} = 0.4$ . In this paragraph we assume that  $\ell_c = 0$ , or in other

489 words we consider that the rock microstructure is homogeneous (see section 3.3). This  
 490 assumption does not influence the conditions for the onset of the compaction band formation (see  
 491 Eqs. (42) or (43)), which is the purpose of the current paragraph. In the next paragraph the  
 492 heterogeneity of the REV will be considered and its influence to compaction bands  
 493 thickness/periodicity will be explored.

494  
 495 According to Eq.(42) compaction band triggering depends on  $\Xi$ , which represents the tendency  
 496 of the system for compaction band formation. With higher values of  $\Xi$ , the region of instability  
 497 in  $q-p$  plane becomes larger. Figure 5 and Figure 6 show the dependency of  $\Xi$  on the grain  
 498 fracturing coefficient  $a$  for  $n = 0.25$  and on the porosity  $n$  for  $a = 0.1$  respectively. Notice that  
 499 when the solution is saturated,  $w_2^h = 1$  (i.e. the dissolution process stops), compaction bands can

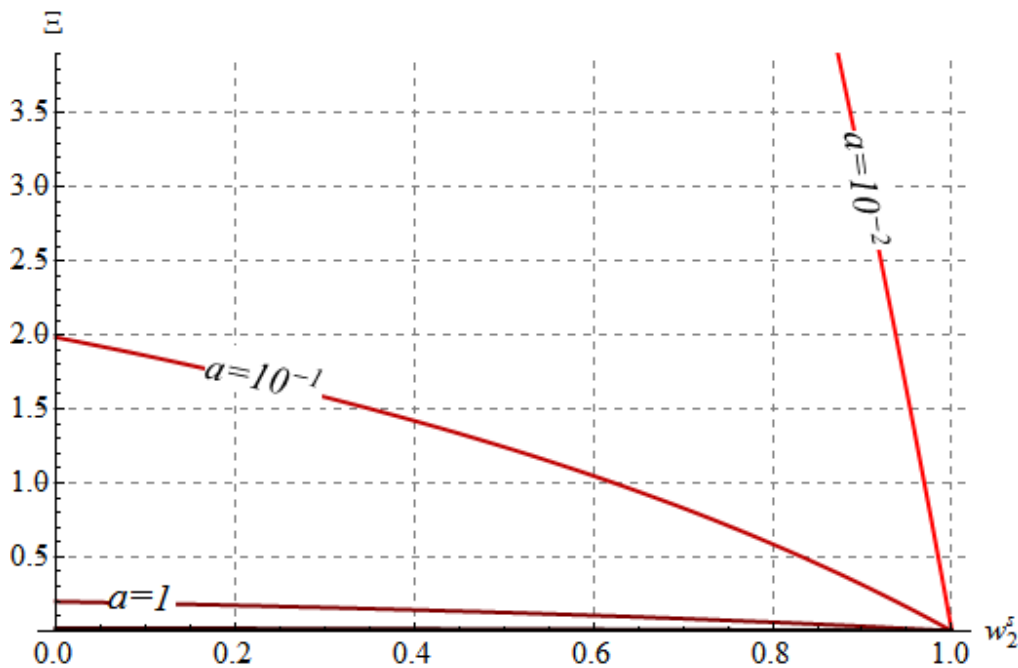
500 be triggered only if  $\beta = -\frac{\sqrt{3}}{2}$  or  $\mu = -\frac{\sqrt{3}}{2}$ . This is consistent with the Issen and Rudnicki

501 condition for compaction bands [Issen and Rudnicki, 2000]. The same holds when no grain  
 502 damage occurs ( $a \rightarrow \infty$ ) or when the medium is not porous ( $n \rightarrow 0$ ), as no reaction takes place

503 and chemical softening is impossible. According to Figure 6, in the case of layered materials,  
 504 compaction bands would preferentially develop in the more porous layers.

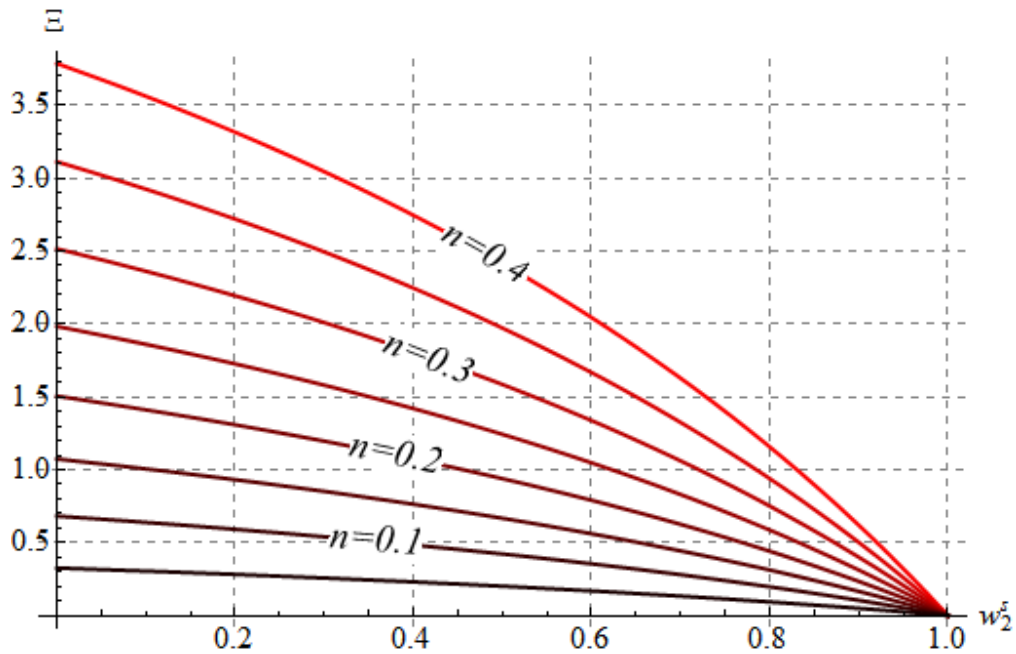
505  
 506 Figure 7, Figure 8 and Figure 9 show the region of instability in the  $q-p$  plane for various  
 507 values of the grain damage coefficient,  $a$ , for  $w_2^h = 0$  and for  $n = 0.25$ . If at a certain time the  
 508 stress state in the  $q-p$  plane is inside this instability region then compaction bands instabilities are  
 509 triggered. Notice that because of the strong chemo-mechanical coupling of the proposed model,  
 510 the instability manifold is larger than the instability manifold defined by the Issen & Rudnicki  
 511 [2000] compaction band criterion (see Figure 7 to Figure 9) and its size depends on the grain  
 512 damage parameter  $a$ . Moreover, compaction bands can be triggered even for  $\beta + \mu > -\sqrt{3}$ .  
 513 Figure 10 shows the growth coefficient  $s$  as a function of the wavelength of the perturbation for  
 514  $a = 10^{-2}$ ,  $w_2^h = 0$ ,  $n = 0.25$ ,  $p = 1.2$ ,  $q = 0.4$  and  $\zeta = 1$ .  $s$  is positive and the system is unstable.

515



516

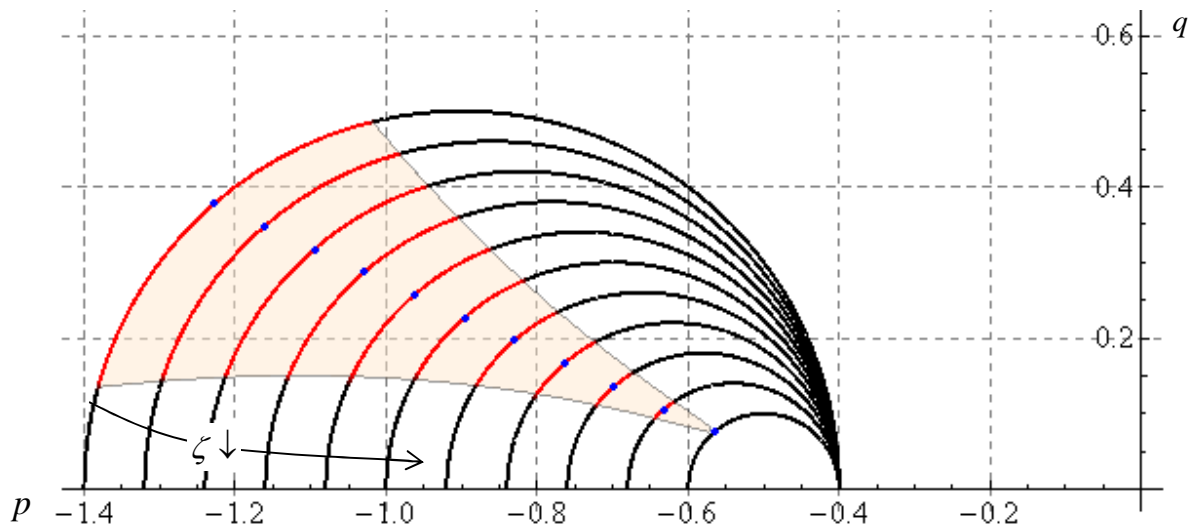
517 *Figure 5. Tendency for compaction bands for  $n = 0.25$ . The more crushable the grains are, i.e.*  
 518  *$a$  small, the bigger the coefficient  $\Xi$  and the larger the region of instability is in  $q-p$  plane.*



519

520 *Figure 6. Tendency for compaction bands for  $a = 0.1$ . The more porous the geomaterial is, the*  
 521 *bigger the coefficient  $\Xi$  and the larger the region of instability in  $q - p$  plane are.*

522

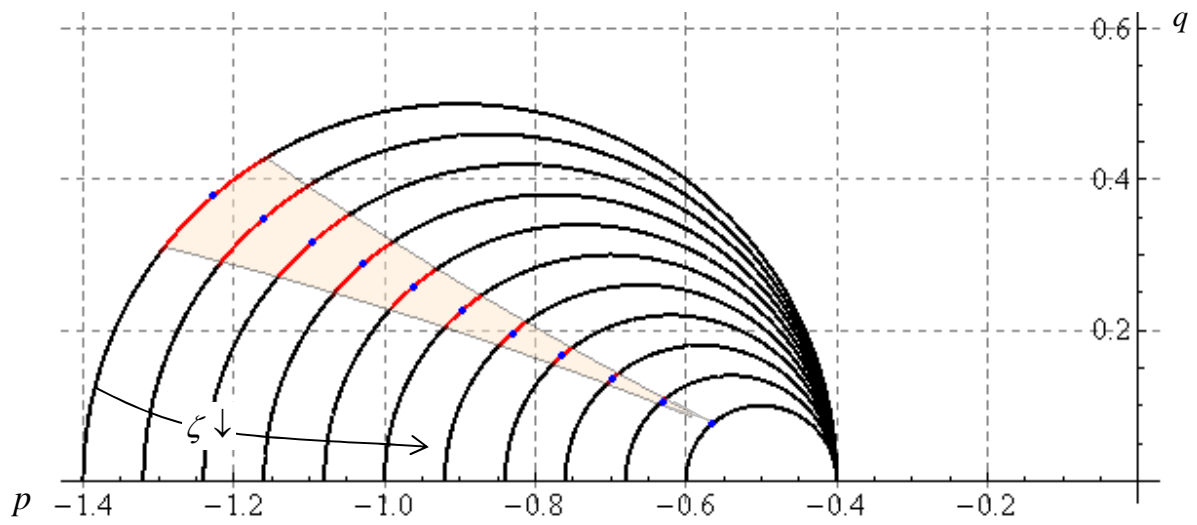


523

524 *Figure 7. Instability region (shaded) for compaction bands under oedometric conditions for*  
 525  *$a = 10^{-3}$  ( $\Xi = 200$ ). The points (in blue) represent the Issen & Rudnicki criterion for compaction*  
 526 *band instabilities. Different yield surfaces are drawn for different levels of chemical degradation*  
 527  *$\zeta$ .*

528

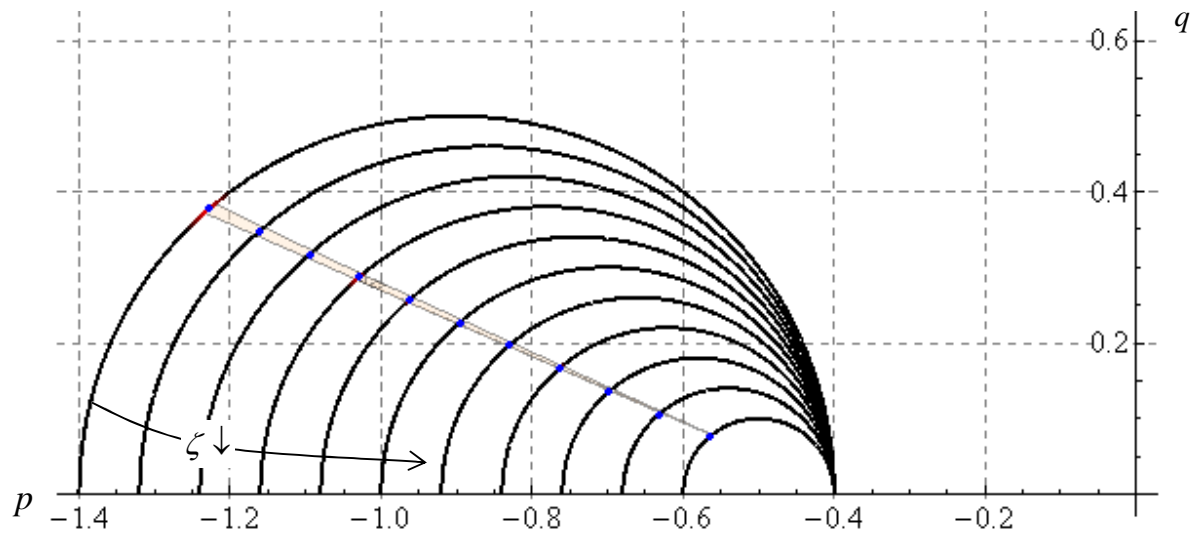
529



530

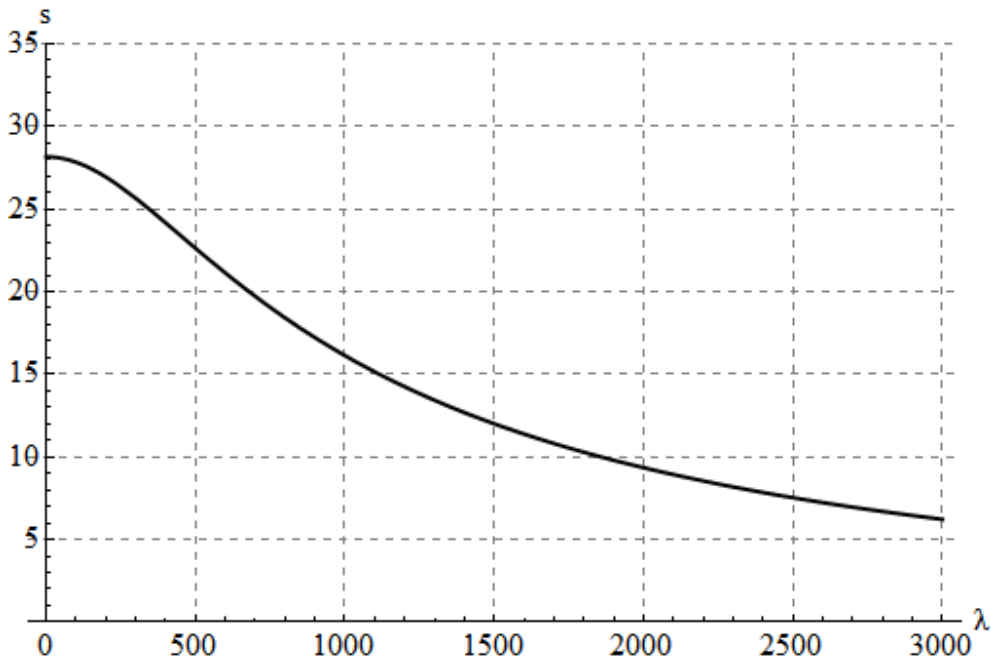
531 *Figure 8. Instability region (shaded) for compaction bands under oedometric conditions for*  
 532  *$a = 10^{-2}$  ( $\Xi = 20$ ). The points (in blue) represent the Issen & Rudnitsky criterion for*  
 533 *compaction band instabilities. Different yield surfaces are drawn for different levels of chemical*  
 534 *degradation  $\zeta$ .*

535



536

537 *Figure 9. Instability region (shaded) for compaction bands under oedometric conditions for  $a = 1$*   
 538 *( $\Xi = 2$ ). The points (in blue) represent the Issen & Rudnitsky criterion for compaction bands.*  
 539 *Different yield surfaces are drawn for different levels of chemical degradation  $\zeta$ .*



540

541 *Figure 10. Instability growth coefficient  $s$  in terms of the perturbation wavelength  $\lambda$  for  $\ell_c = 0$ .*  
 542 *The growth coefficient is positive and the system is unstable.*

543

#### 544 **4.4. Wave length selection**

545 Figure 10 shows that the perturbation that travels fastest (maximum growth coefficient -  
 546 dominant wave length) has zero wavelength. In other words, the dominant wavelength,  $\lambda_{\max}$ , is  
 547 zero. This means that the deformation would be localized in a zone of an infinitesimal thickness  
 548 as time increases (see Eq.(33)) or equivalently that the compaction bands would be  
 549 infinitesimally close to each other ( $spacing = \lambda_{\max} = L_b/N = 0$  and so for given  $L = L_b$ ,  $N \rightarrow \infty$ ).  
 550 However, experimental evidence shows that this is hardly the case. Due to the heterogeneous  
 551 microstructure of geomaterials, compaction is localized to a thin band of finite thickness (several  
 552 grains). Consequently, the evolution of the reaction cannot be homogeneous over the REV (  
 553  $\ell_c \neq 0$ , Eq.(26)). For example, assuming, that the REV has a size of  $\ell_{REV} = 20$  (twenty grains),  
 554 then  $\ell_c \simeq 4$ . The size of the REV is rather a statistical quantity and depends on the material at  
 555 hand. For the aforementioned characteristic length, the linear stability analysis shows that the  
 556 perturbation that travels fastest has a wave length equal to approximately  $\lambda_{\max} = 160$  grains

557 (Figure 11) leading to a thickness of 80 grains for the compaction band ( $\frac{\lambda_{\max}}{2} = 80D_0^{50}$ ) or  
 558 equivalently to a finite minimum compaction band spacing ( $spacing = \lambda_{\max} = L_b/N$  for given  
 559  $L = L_b$ ). The derived compaction band thickness refers to the compressive part of the  
 560 perturbation which is half of the wavelength. For  $D_0^{50} = 0.1\text{mm}$  the thickness of the band is 8  
 561 mm.

562  
 563 In the literature, field and laboratory observations show that the thickness of deformation bands is  
 564 variable. Tondi [2007] presents the example of a quite thick compactive shear band of the order  
 565 of 300 grains. On the contrary, in Baud et al. [2004], the thickness of the compaction band  
 566 observed is of the order of two grains. In the present analysis the compaction band thickness  
 567 depends on the chemo-mechanical properties of the material and of the heterogeneity of the  
 568 microstructure. However, it should be mentioned that the present model should not be considered  
 569 as predictive and that the calculated compaction band thickness has only a qualitative character.  
 570 In particular, the derived compaction band thickness corresponds to the thickness of the  
 571 compacting zone at the onset of the localization. This process zone may decrease further during  
 572 compaction. For example, strain softening because of grain crushing/fracturing and pore collapse,  
 573 which was excluded here in order to isolate the effects of dissolution, can decrease further the  
 574 compaction band thickness. In order to simulate the evolution of the compaction band thickness,  
 575 a post-bifurcation analysis is necessary which exceeds the scope of the present paper.

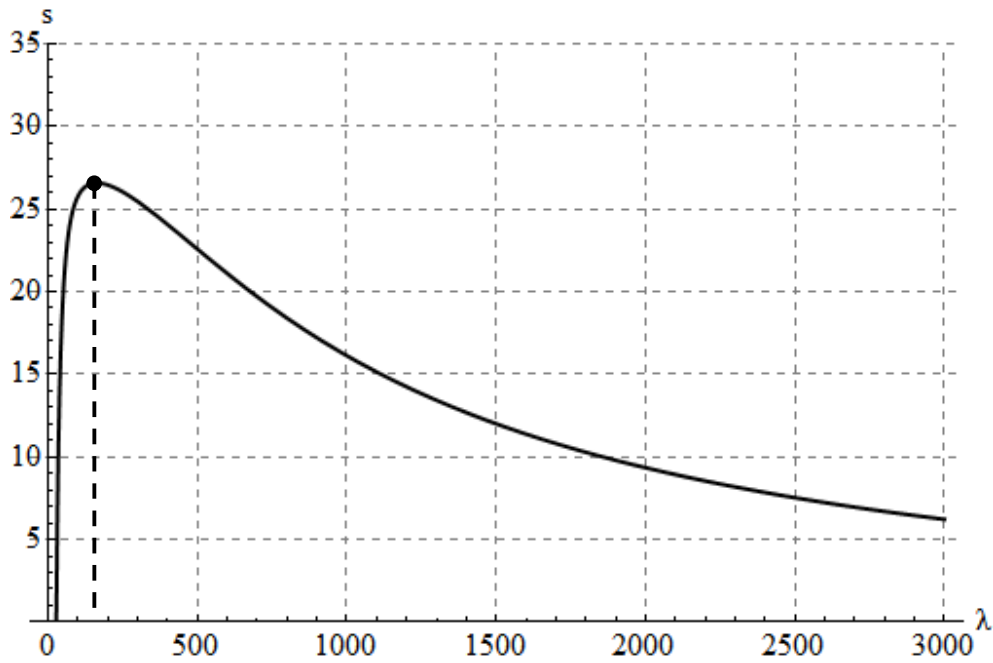
576  
 577 The dominant wavelength,  $\lambda_{\max}$ , depends on the hydraulic diffusivity of the rock. In Figure 12  
 578 we trace the Lyapunov exponent,  $s$ , versus the wavelength  $\lambda$  for different orders of magnitude of  
 579 the hydraulic diffusivity. The lowest considered value of the dimensionless hydraulic diffusivity  
 580  $c_{hy}$  is  $6 \times 10^3$  and the highest is  $6 \times 10^{10}$ . These values correspond to permeability values ranging  
 581 from  $10^{-13} \text{m}^2$  to  $10^{-20} \text{m}^2$ . Figure 12 shows that a lower permeability of the material leads to a  
 582 smaller dominant wavelength. In other words, the present model leads to thinner compaction  
 583 bands for more impermeable materials. From the physical point of view, at the onset of the  
 584 instability, chemical dissolution leads locally to an abrupt increase of the plastic deformations  
 585 and an abrupt reduction of the effective vertical stress. In oedometric conditions, this drop of the

586 vertical effective stress leads to a fast increase of the pore pressure inside the compaction band in  
587 order to equilibrate the total applied vertical stress, which is assumed constant. Therefore, the role  
588 of hydraulic diffusivity is crucial, as a more permeable material would need a larger zone in order  
589 for the pore pressure to rapidly increase and equilibrate the constant total vertical stress. On the  
590 contrary, in a less permeable material, this zone will be narrower leading to thinner compaction  
591 bands. Moreover, the faster the dissolution reaction is, the more rapidly the pore pressure has to  
592 build-up in order to equilibrate the total vertical stress. Consequently, for a given value of the  
593 hydraulic diffusivity parameter, the chemical softening rate controls the thickness of the  
594 localization zone.

595  
596 The chemical softening rate depends on the grain damage parameter  $a$  and on the dissolution  
597 rate  $k^*$ . Figure 13 shows the dependency of the compaction band thickness on the grain damage  
598 parameter for the numerical example presented in the previous section. As expected, stronger  
599 grain damage (i.e. lower values of parameter  $a$ ) leads to thinner bands (a higher specific surface  
600 leads to a higher chemical softening rate). It should be emphasized, though, that this is only a  
601 chemical softening effect and that the possible introduction of additional mechanical softening  
602 through grain breakage would enhance this trend. Similarly, in Figure 14 we present the  
603 dominant wavelength in terms of the grain damage parameter for various orders of magnitude of  
604 the dissolution rate coefficient. We observe that a faster reaction rate leads to a narrower  
605 compaction band at the onset of the localization. This is due to the fact that higher values of  $k^*$   
606 increase the chemical softening rate (Eq.(22) and (23)). Alternatively, the impact of the  
607 dissolution rate to strain localization can be investigated through the non-dimensional expression  
608 of the hydraulic diffusivity parameter. According to equation (27) by increasing the dissolution  
609 rate (faster reaction) the non-dimensional hydraulic diffusivity decreases, which leads to thinner  
610 compaction bands as discussed above (Figure 12).

611  
612 These mathematical results have to be experimentally verified. In absence of experimental  
613 evidence, one could however remark that it is consistent with what is observed for shear bands  
614 where the localization zone decreases with increasing mechanical or chemical softening  
615 [*Vardoulakis and Sulem, 1995; Sulem et al., 2011; Brantut and Sulem, 2012; Veveakis et al.,*  
616 *2012, 2013*]. In the present case, the dissolution increases the chemical softening of the material.

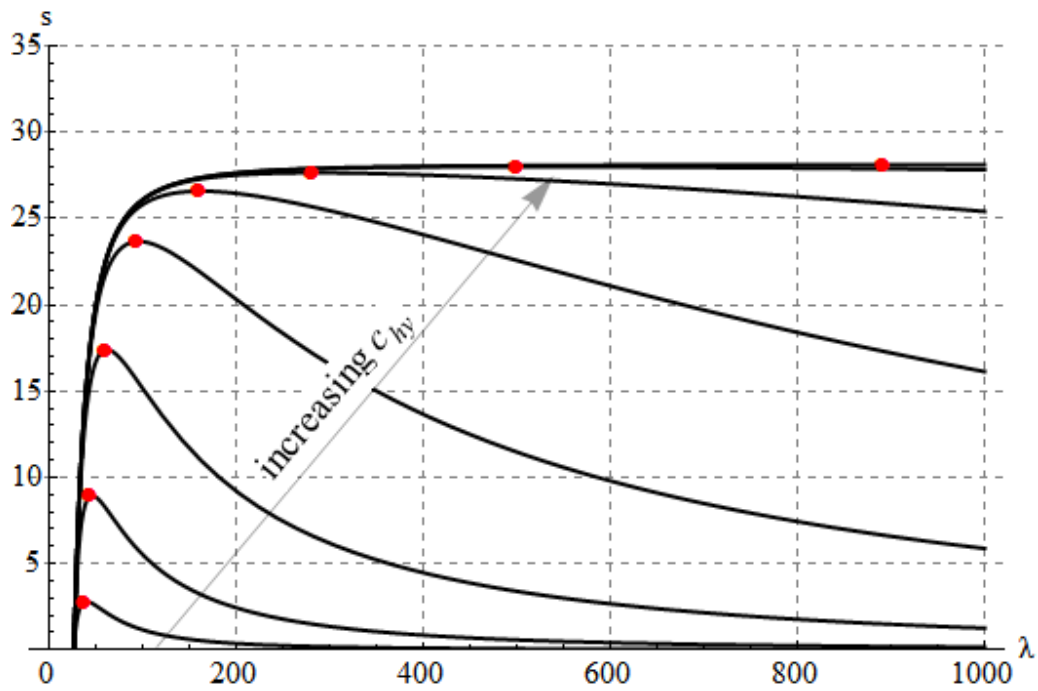
617 The deformation rate is linked to the dissolution rate so that a faster dissolution induces a higher  
 618 softening rate.



619

620 *Figure 11. Growth coefficient,  $s$ , in terms of the perturbation wave length for  $a = 10^{-2}$  and*  
 621  *$\ell_c \simeq 4$ . The dominant wave length corresponds to the value of  $\lambda$  for which the growth*  
 622 *coefficient is maximum. The thickness of the compaction band is proportional to the dominant*  
 623 *wave length.*





624

625 *Figure 12. Influence of hydraulic diffusivity on the dominant wavelength for  $a = 10^{-2}$  and  $\ell_c \approx 4$ .*  
 626 *The red dots represent the maximum value of the Lyapunov exponent for a given hydraulic*  
 627 *diffusivity. The more impermeable the medium is the more localized the compaction instability*  
 628 *becomes (smaller wavelength).*

629

630

631

632

633

634

635

636

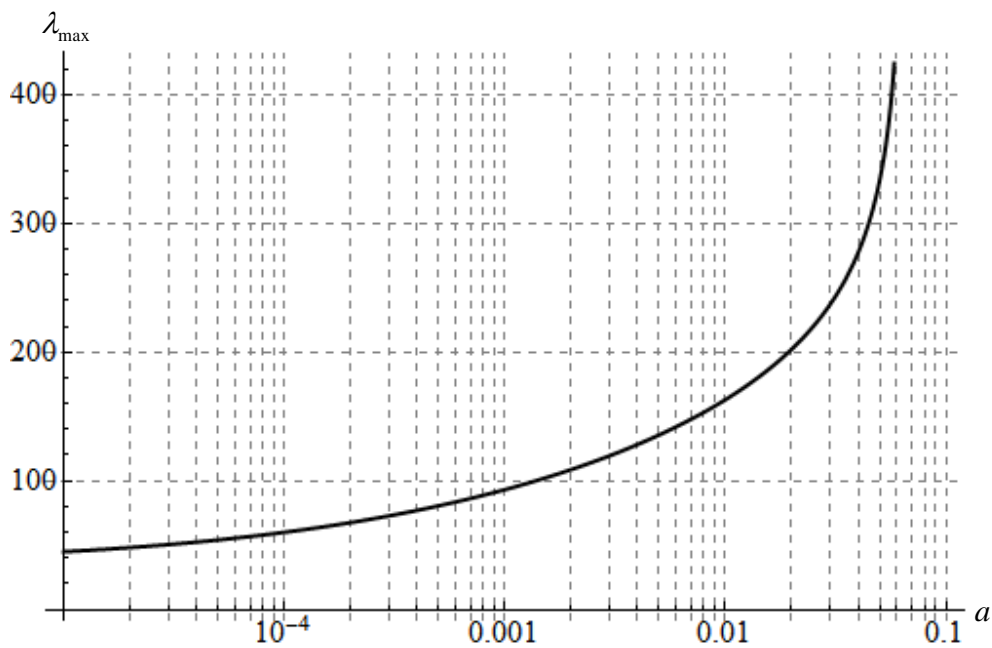
637

638

639

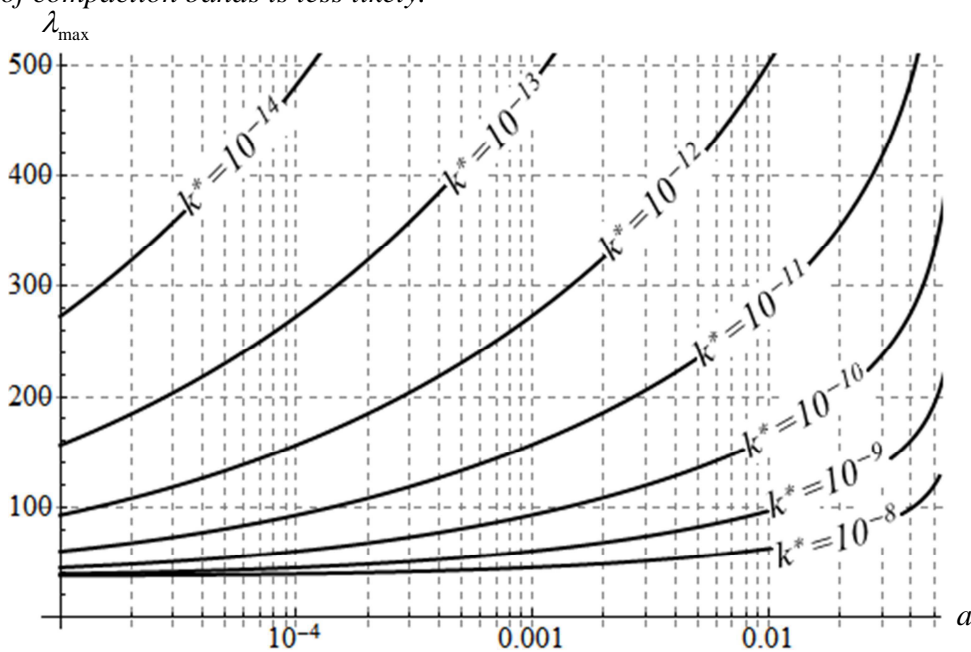
640

641



642

643 *Figure 13. Dominant wave length (wave length selection) in terms of the grain damage*  
 644 *parameter  $a$ . As the grains become less crushable,  $\lambda_{\max}$  tends to infinity and therefore the*  
 645 *formation of compaction bands is less likely.*



646

647

648 *Figure 14. Dominant wave length (wave length selection) in terms of the grain damage*  
 649 *parameter  $a$  for various values of the dissolution rate ( $k^*$  in m/s). The faster the reaction is the*  
 650 *narrower the compaction band zone is.*

651 **5. Case studies**652 **5.1. Compaction banding of a sandstone reservoir**

653 The scenario of water flooding of a sandstone reservoir at 4km depth is studied in this paragraph.

654 This example could reflect the conditions of enhanced oil recovery by injecting water into the

655 reservoir to maintain the pore pressure. In offshore operations the injected water is commonly

656 seawater, which is different from the formation water. The injection of water can trigger the

657 dissolution of the quartz-based rock (R1) which in turn may trigger compaction band instabilities.

658 At this depth it is assumed that the water pressure is  $p_f \approx 40\text{MPa}$  and the total vertical stress is659  $\sigma_n \approx 100\text{MPa}$ . Some typical values for sandstone are given in Table 1.

660

661 *Table 1. Indicative material properties of the sandstone.*

Quantity	Value	Dimensionless value
Hydraulic diffusivity, $c_{hy}$	$2 \cdot 10^{-3} \text{ m}^2 \text{ s}^{-1}$	$6.25 \cdot 10^{11}$
Grain diameter, $D_0^{50}$	0.1 mm	1
Effective grain surface area to volume ratio, $S$	$50 \text{ mm}^{-1}$	1
Bulk modulus, $K$	10 GPa	100
Shear modulus, $G$	7.5 GPa	75
Porosity, $n$	0,20	-
CSL slope, $M$	1	-
Initial yield stress, $p'_0$	60 MPa	0.60
Residual yield stress, $p'_R$	15 MPa	0.15
Chemical Softening exponent, $\kappa$	2	-
Grain damage parameter, $a$	0.5 MPa	0.005
$\mu_3/\mu_2$	0,6	-
Fluid density, $\rho_f$	$1 \text{ g cm}^{-3}$	1
Solid density, $\rho_s$	$2.65 \text{ g cm}^{-3}$	2.65
Dissolution rate, $k$	$10^{-8} \text{ mol s}^{-1} \text{ m}^{-2}$ ( $k^* \approx 10^{-12} \text{ m/s}$ )	

662

663 Before the reaction takes place the stress state is represented by the point A in the  $q-p$  plane

664 (Figure 15). Elastic loading under oedometric conditions is assumed for the initial stress state, i.e.

665 point A (stress path line no. 1) and  $\sigma_{zz} = -\sigma_n = -100\text{MPa}$ . At time  $t = 0$  the reservoir is flooded  
 666 with water. The water injected in the reservoir is continuously renewed in such a way that  
 667 practically open flow conditions hold ( $w_2(t > 0) = 0$ ). As a result the system is not in chemical  
 668 equilibrium and dissolution occurs. Consequently, the material is progressively degraded due to  
 669 chemical softening and the chemical softening parameter decreases from its initial value  $\zeta_0 = 1$ .  
 670 When  $\zeta = \zeta_A \approx 0.9$  the material yields, plastic strains are accumulated and grain damage occurs  
 671 (Eq.(19)). By neglecting in this phase the influence of the dissolution on the increase of the  
 672 specific area of the grains of the rock (i.e. effective grain surface area to grain volume ratio,  $S$ , is  
 673 assumed quasi-constant) an estimation of the time needed for yielding is possible. Equations (22)  
 674 and (23) are combined to give, for sub-spherical grains:

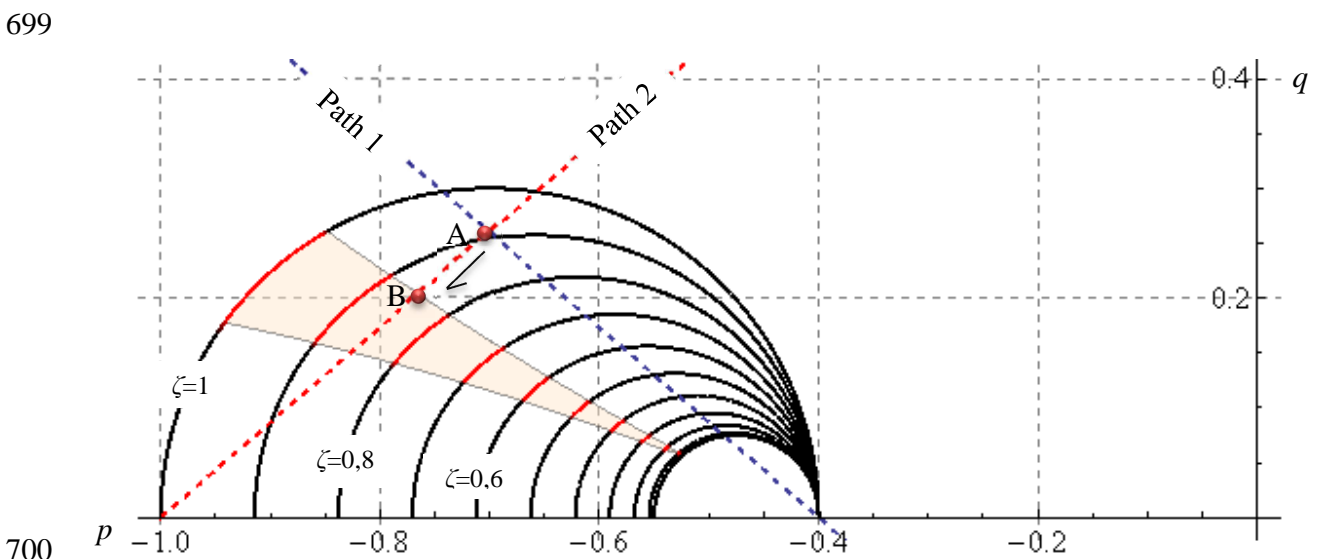
$$675 \quad t_A \approx \frac{\mu_2 \rho_s}{\mu_3 \rho_f} \frac{1}{S k^*} \ln \zeta_A^{-1} \approx 3.5 \text{ months} \quad (46)$$

676 It should be mentioned that if closed flow conditions were considered ( $w_2(t = 0) = 0$ ,  
 677  $w_2(t > 0) \neq 0$ ) then the dissolution would be slower and several injection cycles would be  
 678 needed for yielding as the solution saturates quite quickly (equilibrium constant:  $\log K_{eq} \approx -3.15$   
 679 at  $80^\circ\text{C}$ ) without provoking significant chemical softening.

680  
 681 After reaching point A, the yield surface continues to contract due to dissolution and the stress  
 682 state evolves until point B. At point B the system becomes unstable and compaction band  
 683 instabilities are triggered. The minimum thickness of the compaction bands is equal to  $\pi \ell_c$   
 684 (Eq.(42)), but this can be larger depending on the exact stress path, the chemo-mechanical  
 685 parameters (paragraph 4.4) and the nonlinear behavior of the system in the post bifurcation  
 686 regime. Contrary to the post bifurcation regime, where the deformations are abruptly localized  
 687 and the conditions can be considered undrained, drained conditions can be assumed from point A  
 688 to point B if we consider that the time scale of the pore fluid diffusion is much faster than the  
 689 time scale of the chemical softening process. Therefore, we can admit that the stress path after  
 690 yielding follows Path 2 (Figure 15). This path is derived from the fact that the vertical stress is  
 691 kept constant  $\sigma_{zz} = -\sigma_n$  under oedometric conditions (see Eq.(16)).

692

693 The instability happens when  $\zeta = \zeta_B \approx 0.85$ . From point A to point B the specific surface of the  
 694 grains is smoothly increased as microcracking, debonding and grain crushing take place  
 695 (homogeneous accumulation of plastic deformations, Eq.(19)). Assuming for simplicity that  
 696  $S_B \approx S_A$ , the time needed for instability ( $\zeta_0 \rightarrow \zeta_B$ ) is of the order  $t_B \approx 5$  months. After this  
 697 point the deformations are localized into a zone of finite thickness (Eq.(42)) and excessive grain  
 698 damage occurs (onset of instability – compaction band formation).



701 *Figure 15. Instability region (shaded) for compaction bands under oedometric conditions for a*  
 702 *sandstone at 4 km depth. Different yield surfaces are drawn for different levels of chemical*  
 703 *degradation,  $\zeta$ . The stress path 1 represents the elastic loading of the material under*  
 704 *oedometric conditions, while the stress path 2 represents the path that the material follows after*  
 705 *yielding.*

706

## 707 **5.2. Compaction banding induced by $CO_2$ injection in carbonate grainstones**

708 The formation of compaction bands in carbonate rocks is hardly evidenced both in field and in  
 709 laboratory [Baud *et al.*, 2009]. Nevertheless, more recently, Cilona *et al.* [2012] observed  
 710 compaction bands in porous carbonate grainstones both in field and in laboratory. Their  
 711 observations extend the previous evidence of compaction bands in porous carbonate rocks by  
 712 Baxevanis *et Papamichos* [2006] and Tondi *et al.* [2006]. In the aforementioned works, Hertzian  
 713 cracks at grain contacts, microcracking, debonding and pore collapse that result in an overall  
 714 effective grain size reduction were shown to develop inside compaction bands. As it was

715 mentioned in paragraph 3.2, these mechanisms are essentially taken into account in the proposed  
 716 model through the hyperbolic fit of the evolution of the effective grain size with the mechanical  
 717 energy input into the system (Eqs. (18), (19)).

718  
 719 In this paragraph we attempt to explore the possibility of compaction bands formation in  
 720 carbonate grainstones because of CO<sub>2</sub> injection at 1.8 km depth. The set of reactions that take  
 721 place because of the CO<sub>2</sub> injection are summarized through the stoichiometry of equation R2. In  
 722 Table 2 we present some typical values for the chemo-mechanical parameters of a porous  
 723 carbonate rock. At this depth, we assume that the water pressure is  $p_f \approx 18\text{MPa}$  and the total  
 724 vertical stress is  $\sigma_n \approx 45\text{MPa}$ . The instability region, the elastic and plastic oedometric stress  
 725 paths as well as the initial stress state (Point A) are shown in Figure 16. Following the same  
 726 reasoning as in the previous case study, a CO<sub>2</sub> solution is injected in the rock mass. The rock  
 727 dissolves and its mechanical strength diminishes (open fluid flow conditions). When  
 728  $\zeta = \zeta_A \approx 0.9$  the rock starts to yield and a homogeneous plastic strain field is developed. This  
 729 phase of deformation under constant applied loading (i.e. the overburden) corresponds to the  
 730 creep behavior that is observed due to CO<sub>2</sub> injection [*Le Guen et al.*, 2007; *Liteanu and Spiers*,  
 731 2009; *Rutqvist*, 2012]. At point B (Figure 16),  $\zeta = \zeta_B \approx 0.63$ , the system bifurcates and  
 732 compaction bands are formed. Again the minimum thickness (or spacing) of the compaction  
 733 bands is equal to  $\pi\ell_c$  (Eq.(42)), but this can be different depending on the stress path, the  
 734 chemo-mechanical parameters and the nonlinear behavior of the system in the post bifurcation  
 735 regime (mechanical softening).

736  
 737 Under open flow conditions, an estimation for the time needed for reaching point B is  $t_B \approx 5$  days  
 738 (Eq.(46) assuming a constant value for  $S$  until the instability and sub-spherical grains). Notice,  
 739 that this period of time is far smaller as compared to the previous example due to the faster  
 740 dissolution rate of calcite.

741  
 742 For CO<sub>2</sub>, injection open flow conditions would correspond to a zone outside the gas plume where  
 743 the formation fluid is saturated with CO<sub>2</sub>, but is not in chemical equilibrium with the rock so that

744 carbonate dissolution occurs continuously ( $w_2 < w_2^{eq}$ ). Rohmer and Seyedi [2010], using an  
 745 hydro-mechanical model on a reservoir case study, show that the dissolution front might extend  
 746 few kilometers around the injection well after 10 years of continuous injection.

747

748 Table 2. Indicative material properties of a carbonate grainstone.

Quantity	Value	Dimensionless value
Hydraulic diffusivity, $c_{hy}$	$10^{-3} \text{ m}^2 \text{ s}^{-1}$	$3 \cdot 10^5$
Grain diameter, $D_0^{50}$	0.2 mm	1
Effective grain surface area to volume ratio, $S$	$25 \text{ mm}^{-1}$	1
Bulk modulus, $K$	5 GPa	110
Shear modulus, $G$	5 GPa	110
Porosity, $n$	0.25	-
CSL slope, $M$	0.9	-
Initial yield stress, $p'_0$	30 MPa	0.67
Residual yield stress, $p'_R$	0 MPa	0
Chemical Softening exponent, $\kappa$	1	-
Grain crushing parameter, $a$	1 MPa	0.011
$\mu_3/\mu_2$	0.62	-
Fluid density, $\rho_f$	$1 \text{ g cm}^{-3}$	1
Solid density, $\rho_s$	$2.65 \text{ g cm}^{-3}$	2.65
Dissolution rate, $k$	$10^{-6} \text{ mol s}^{-1} \text{ m}^{-2}$ ( $k^* \approx 1.6 \cdot 10^{-10} \text{ m/s}$ )	

749

750

751

752

753

754

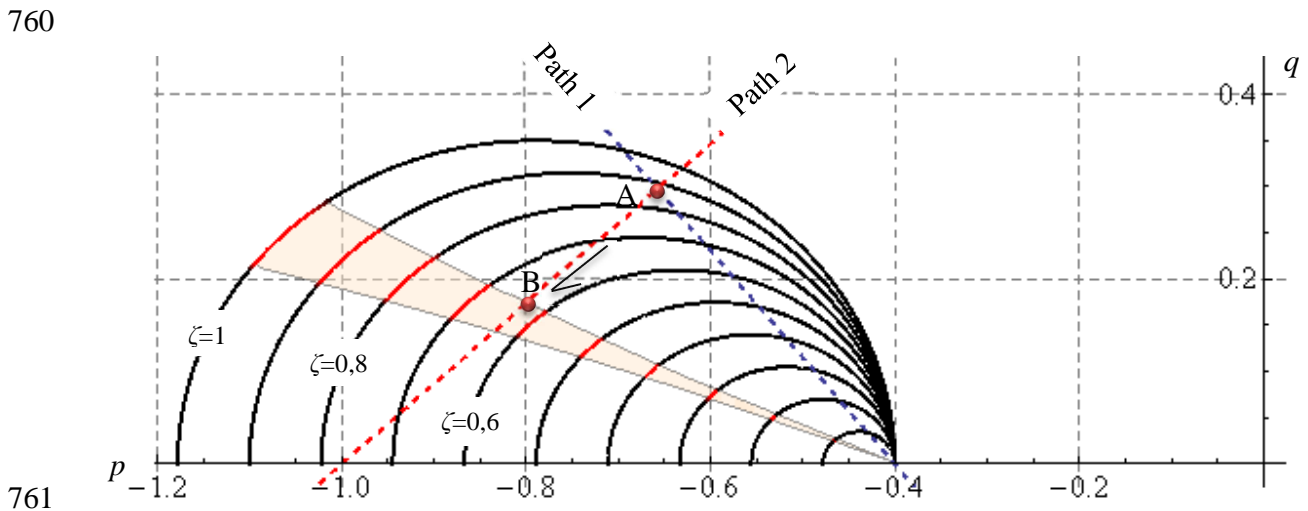
755

756

757

758

759



762 *Figure 16. Instability region (shaded) for compaction bands under oedometric conditions for a*  
 763 *carbonate grainstone at 1.8 km depth. Different yield surfaces are drawn for different levels of*  
 764 *chemical degradation,  $\zeta$ . The stress path line no. 1 represents the elastic loading of the material*  
 765 *under oedometric conditions, while the stress path line no. 2 represents the path that the material*  
 766 *follows after yielding.*

767

## 768 6. Conclusions

769 Grain fracturing and attrition, “microcracking” of the cementitious matrix, debonding and pore  
 770 collapse are some important micro-mechanisms that lead to the reduction of the effective grain  
 771 size of a geomaterial and consequently to the increase of the dissolution front in reactive  
 772 environments. The proposed chemo-poro-mechanical model accounts for the aforementioned  
 773 mechanisms. Part of the mechanical energy supplied to the system is dissipated through various  
 774 micro-mechanisms for the creation of new surfaces in the microstructure. In this sense, a  
 775 phenomenological approach based on the work of Lade et al. [1996] is used to relate the effective  
 776 grain specific surface and the total energy input per specimen unit volume. Following this  
 777 approach, which describes the above dissipative mechanisms through a single parameter, and in  
 778 the frame of dissolution process, the chemo-poro-mechanical model presented herein provides a  
 779 strong coupling between mechanics and reaction kinetics (Figure 1).

780

781 The purpose of the present paper was to explore the possibility of chemically induced compaction  
 782 band instabilities. Therefore, in order to isolate the chemical effects, mechanical softening



783 induced by grain damage was not considered in the present form of the proposed chemo-poro-  
784 mechanical model. The stability of the system is studied through a linear stability analysis, which  
785 revealed the critical parameters for which compaction bands may occur in quartz- and carbonate-  
786 based rocks. Porosity and grain damage sensitivity (parameter  $a$ ) are important parameters that  
787 considerably influence the triggering of compaction band instabilities due to dissolution. For a  
788 specific rock, the determination of the exact value of the grain damage sensitivity parameter is  
789 possible and may include classical mechanical tests, grain-size analyses and/or microstructural  
790 observations and measurements (e.g. X-ray tomography, acoustic emissions). The other  
791 parameters of the model (elastic constants, yield surface, chemical softening factor and reaction  
792 kinetics) can also be determined experimentally.

793  
794 Due to the existing heterogeneity of the microstructure (e.g. different grain sizes and constituents  
795 in the REV) the dissolution rate may not be homogeneous over the REV. The size of the REV is  
796 a finite statistical quantity that depends upon the geomaterial at hand. Therefore, a rock is  
797 characterized by at least one characteristic length, which by appropriately up-scaling the micro-  
798 level to the macro-level (separation of scales and averaging) can be adequately expressed at the  
799 macroscale, i.e. incorporated into the proposed chemo-poro-mechanical model. The linear  
800 stability analysis shows that because of this characteristic length, the deformation is localized into  
801 narrow bands of finite thickness and that these bands are periodically distributed in space. This is  
802 in accordance with many field and laboratory observations where there is evidence that  
803 compaction bands are localized into a thin band (several grains thickness) and are quasi-  
804 periodically arranged in space. In field and laboratory observations, the thickness of compaction  
805 bands is variable. In the present analysis the compaction band thickness depends on the chemo-  
806 poro-mechanical properties of the material and the heterogeneity of the microstructure.  
807 According to the present model, the thickness and the periodicity of compaction bands are related  
808 to the grain damage parameter, the hydraulic diffusivity and the dissolution rate. The more  
809 crushable the grains are, the lower the permeability is and the higher the dissolution rate is, the  
810 narrower the compaction band is. Nevertheless, the results presented here have a qualitative  
811 character. The study of the precise evolution of the system and of the compaction band thickness  
812 after the onset of localization (post-bifurcation regime) exceeds the scope of the present paper

813 and will be pursued further in a future work by integrating the non-linear chemo-poro-mechanical  
814 system of equations.

815

816 Finally, two scenarios of chemically induced compaction band instabilities were investigated.  
817 The first one concerns the water flooding of a quartzic rock reservoir, while the second one  
818 concerns a carbonate grainstone in which a CO<sub>2</sub> solution is injected. The effect of open and  
819 closed flow conditions was discussed, the instability regions were determined and a rough  
820 estimation of the critical time for compaction band triggering was made. Two phases are  
821 distinguished. The first phase is characterized by a creep behavior of the rock, while in the  
822 second phase compaction band instabilities are triggered. The present study focused on pure  
823 compaction bands, but the concept of the present model can be extended to other types of  
824 deformation bands, such as shear bands. The formation of deformation bands in reservoirs due to  
825 chemical processes and other non-linearities can be related to important changes in permeability,  
826 to the creation of reinforced zones (compactive behavior) or, in the contrary, to the creation of  
827 new faults and fractures (shear behavior). However, in order to quantify the implications of such  
828 phenomena to the sustainability of reservoir projects, large scale simulations are necessary that  
829 will take into account the aforementioned phenomena and the precise injection characteristics.

## 830 **7. Acknowledgements**

831 The authors would like to acknowledge the associate editor and the anonymous reviewers for  
832 their fruitful comments and suggestions, which improved the paper. Moreover, they would like to  
833 acknowledge the support of the French National Agency for Research (ANR FISIC n° ANR-11-  
834 SEED-0003).

## 835 **8. Appendix**

### 836 **8.1. *Reaction kinetics in terms of mass fraction and specific area***

837 At the microscale the mass fraction is:

838 
$$w_2 = \frac{m_2}{m_f} \text{ or } w_2 = \frac{\mu_2}{\rho_f V_f} n_2 \quad (\text{A1})$$

839 where  $m_f$  is the mass of the fluid phase and  $m_2$  is the mass of the dissolution product at the  
 840 microscale. Assuming that  $w_2 \ll 1$  or equivalently that the density of the fluid,  $\rho_f$ , remains  
 841 practically constant during the reaction process, we obtain that:

842 
$$\frac{\partial n_2}{\partial t} \approx \frac{\rho_f}{\mu_2} e V_s \frac{\partial w_2}{\partial t} \quad (\text{A2})$$

843 Furthermore, assuming that the activity coefficients for the reactants are close to unity the  
 844 reaction quotient is expressed in terms of the reaction activities of the reactants as follows:

845 
$$Q \approx \frac{a_2}{a_1} \text{ or } Q \approx \frac{n_2}{n_1} \quad (\text{A3})$$

846 Assuming again that  $w_2 \ll 1$ , we obtain:

847 
$$Q \approx w_2 \frac{\mu_1}{\mu_2} \quad (\text{A4})$$

848 Consequently the mass fraction at equilibrium is related to the equilibrium constant as follows:

849 
$$w_2^{eq} \approx \frac{\mu_2}{\mu_1} K_{eq} \quad (\text{A5})$$

850 Using the above expressions, Eq.(20) yields:

851 
$$\frac{\partial w_2}{\partial t} \approx k \frac{\mu_2}{\rho_f} \frac{S}{e} \left( 1 - \frac{w_2}{w_2^{eq}} \right) \quad (\text{A6})$$

852 where we set  $S = \frac{A}{V_s}$ .

853 **8.2. Chemical softening parameter and mass fraction**854 By definition  $\zeta = \frac{M_s}{M_s^0}$  and using the stoichiometry of the dissolution reaction we obtain:

855 
$$\frac{\partial \zeta}{\partial t} = \frac{1}{M_s^0} \frac{\partial M_s}{\partial t} = -\frac{\mu_3}{M_s^0} \frac{\partial n_2}{\partial t} \quad (\text{A7})$$

856 Using Eq.(A2) at the macroscale (REV) we get for  $w_2^M \ll 1$  :

857 
$$\frac{\partial \zeta}{\partial t} \approx -\frac{\mu_3}{\mu_2} \frac{M_f}{M_s^0} \frac{\partial w_2^M}{\partial t} = -\frac{\mu_3}{\mu_2} \frac{\rho_f}{\rho_s} e \frac{M_s}{M_s^0} \frac{\partial w_2^M}{\partial t} \quad (\text{A8})$$

859 or

860 
$$\frac{\partial \zeta}{\partial t} \approx -\frac{\mu_3}{\mu_2} \frac{\rho_f}{\rho_s} e \zeta \frac{\partial w_2^M}{\partial t} \quad (\text{A9})$$

861

862 **9. References**863 Aydin, A., and R. Ahmadov (2009), Bed-parallel compaction bands in aeolian sandstone: Their  
864 identification, characterization and implications, *Tectonophysics*, 479(3-4), 277–284,  
865 doi:10.1016/j.tecto.2009.08.033.866 Baud, P., E. Klein, and T. Wong (2004), Compaction localization in porous sandstones: spatial  
867 evolution of damage and acoustic emission activity, *J. Struct. Geol.*, 26(4), 603–624,  
868 doi:10.1016/j.jsg.2003.09.002.869 Baud, P., V. Vajdova, and T. Wong (2006), Shear-enhanced compaction and strain localization:  
870 Inelastic deformation and constitutive modeling of four porous sandstones, *J. Geophys. Res.*,  
871 111(B12), 1–17, doi:10.1029/2005JB004101.872 Baud, P., S. Vinciguerra, C. David, a. Cavallo, E. Walker, and T. Reuschlé (2009), Compaction  
873 and Failure in High Porosity Carbonates: Mechanical Data and Microstructural  
874 Observations, *Pure Appl. Geophys.*, 166(5-7), 869–898, doi:10.1007/s00024-009-0493-2.

- 875 Baxevanis, T., E. Papamichos, O. Flornes, and I. Larsen (2006), Compaction bands and induced  
876 permeability reduction in Tuffeau de Maastricht calcarenite, *Acta Geotech.*, 1(2), 123–135,  
877 doi:10.1007/s11440-006-0011-y.
- 878 El Bied, A., J. Sulem, and F. Martineau (2002), Microstructure of shear zones in Fontainebleau  
879 sandstone, *Int. J. Rock Mech. Min. Sci.*, 39(7), 917–932, doi:10.1016/S1365-  
880 1609(02)00068-0.
- 881 Bigoni, D., and T. Hueckel (1991), Uniqueness and localization—I. Associative and non-  
882 associative elastoplasticity, *Int. J. Solids Struct.*, 28(2), 197–213, doi:10.1016/0020-  
883 7683(91)90205-T.
- 884 Brantut, N., and J. Sulem (2012), Strain Localization and Slip Instability in a Strain-Rate  
885 Hardening, Chemically Weakening Material, *J. Appl. Mech.*, 79(3), 031004,  
886 doi:10.1115/1.4005880.
- 887 Brantut, N., M. J. Heap, P. G. Meredith, and P. Baud (2013), Time-dependent cracking and brittle  
888 creep in crustal rocks: A review, *J. Struct. Geol.*, 52, 17–43, doi:10.1016/j.jsg.2013.03.007.
- 889 Castellanza, R., and R. Nova (2004), Oedometric Tests on Artificially Weathered Carbonatic Soft  
890 Rocks, *J. Geotech. Geoenvironmental Eng.*, 130(7), 728–739, doi:10.1061/(ASCE)1090-  
891 0241(2004)130:7(728).
- 892 Cheung, C. S. N., P. Baud, and T. Wong (2012), Effect of grain size distribution on the  
893 development of compaction localization in porous sandstone, *Geophys. Res. Lett.*, 39(21),  
894 n/a–n/a, doi:10.1029/2012GL053739.
- 895 Cilona, A., P. Baud, E. Tondi, F. Agosta, S. Vinciguerra, A. Rustichelli, and C. J. Spiers (2012),  
896 Deformation bands in porous carbonate grainstones: Field and laboratory observations, *J.*  
897 *Struct. Geol.*, 45, 137–157, doi:10.1016/j.jsg.2012.04.012.
- 898 Coussy, O. (2004), *Poromechanics*, Wiley.
- 899 Croizet, D., F. Renard, and J.-P. Gratier (2013), Compaction and porosity reduction in  
900 carbonates: A review of observations, theory, and experiments, *Adv. Geophys.*, 54, 181–238,  
901 doi:10.1016/B978-0-12-380940-7.00003-2.
- 902 Cubillas, P., S. Köhler, M. Prieto, C. Chaïrat, and E. H. Oelkers (2005), Experimental  
903 determination of the dissolution rates of calcite, aragonite, and bivalves, *Chem. Geol.*,  
904 216(1-2), 59–77, doi:10.1016/j.chemgeo.2004.11.009.
- 905 Das, A., G. D. Nguyen, and I. Einav (2011), Compaction bands due to grain crushing in porous  
906 rocks: A theoretical approach based on breakage mechanics, *J. Geophys. Res.*, 116(B8), 1–  
907 14, doi:10.1029/2011JB008265.

- 908 Ghabezloo, S., and J. Sulem (2008), Stress dependent thermal pressurization of a fluid-saturated  
909 rock, *Rock Mech. Rock Eng.*, 42(1), 1–24, doi:10.1007/s00603-008-0165-z.
- 910 Grgic, D. (2011), Influence of CO<sub>2</sub> on the long-term chemomechanical behavior of an oolitic  
911 limestone, *J. Geophys. Res.*, 116(B7), B07201, doi:10.1029/2010JB008176.
- 912 Le Guen, Y., F. Renard, R. Hellmann, E. Brosse, M. Collombet, D. Tisserand, and J.-P. Gratier  
913 (2007), Enhanced deformation of limestone and sandstone in the presence of high P CO<sub>2</sub>  
914 fluids, *J. Geophys. Res.*, 112(B5), B05421, doi:10.1029/2006JB004637.
- 915 Holcomb, D., J. W. Rudnicki, K. a. Issen, and K. Sternlof (2007), Compaction localization in the  
916 Earth and the laboratory: state of the research and research directions, *Acta Geotech.*, 2(1),  
917 1–15, doi:10.1007/s11440-007-0027-y.
- 918 Hu, L. B., and T. Hueckel (2007a), Coupled chemo-mechanics of intergranular contact: Toward a  
919 three-scale model, *Computers and Geotechnics*, 34(4), 306–327,  
920 doi:10.1016/j.compgeo.2007.02.009.
- 921 Hu, L. B., and T. Hueckel (2007b), Creep of saturated materials as a chemically enhanced rate-  
922 dependent damage process, *Int. J. Numer. Anal. Methods Geomech.*, 31(14), 1537–1565,  
923 doi:10.1002/nag.600.
- 924 Issen, K. a., and J. W. Rudnicki (2000), Conditions for compaction bands in porous rock, *J.*  
925 *Geophys. Res.*, 105(B9), 21529, doi:10.1029/2000JB900185.
- 926 Katsman, R., and E. Aharonov (2006), A study of compaction bands originating from cracks,  
927 notches, and compacted defects, *J. Struct. Geol.*, 28(3), 508–518,  
928 doi:10.1016/j.jsg.2005.12.007.
- 929 Katsman, R., E. Aharonov, and H. Scher (2005), Numerical simulation of compaction bands in  
930 high-porosity sedimentary rock, *Mech. Mater.*, 37(1), 143–162,  
931 doi:10.1016/j.mechmat.2004.01.004.
- 932 Lade, P. V., J. A. Yamamuro, and P. A. Bopp (1996), Significance of Particle Crushing in  
933 Granular Materials, *J. Geotech. Eng.*, 122(4), 309–316, doi:10.1061/(ASCE)0733-  
934 9410(1996)122:4(309).
- 935 Liteanu, E., and C. J. Spiers (2009), Influence of pore fluid salt content on compaction creep of  
936 calcite aggregates in the presence of supercritical CO<sub>2</sub>, *Chem. Geol.*, 265(1-2), 134–147,  
937 doi:10.1016/j.chemgeo.2008.12.010.
- 938 Marketos, G., and M. D. Bolton (2009), Compaction bands simulated in Discrete Element  
939 Models, *J. Struct. Geol.*, 31(5), 479–490, doi:10.1016/j.jsg.2009.03.002.

- 940 Nova, R., R. Castellanza, and C. Tamagnini (2003), A constitutive model for bonded  
941 geomaterials subject to mechanical and/or chemical degradation, *Int. J. Numer. Anal.*  
942 *Methods Geomech.*, 27(9), 705–732, doi:10.1002/nag.294.
- 943 Olsson, W. A., D. J. Holcomb, and J. W. Rudnicki (2002), Compaction Localization in Porous  
944 Sandstone: Implications for Reservoir Mechanics, *Oil Gas Sci. Technol.*, 57(5), 591–599,  
945 doi:10.2516/ogst:2002040.
- 946 Rice, J. R. (1976), The localization of plastic deformation, in *Theoretical and Applied Mechanics*  
947 *(Proceedings of the 14th International Congress on Theoretical and Applied Mechanics)*,  
948 edited by W. T. Koiter, pp. 207–220, NorthHolland Publishing Co., Delft.
- 949 Rimstidt, J. D., and H. L. Barnes (1980), The kinetics of silica-water reactions, *Geochim.*  
950 *Cosmochim. Acta*, 44(11), 1683–1699, doi:10.1016/0016-7037(80)90220-3.
- 951 Rohmer, J., and D. M. Seyed (2010), Coupled Large Scale Hydromechanical Modelling for  
952 Caprock Failure Risk Assessment of CO<sub>2</sub> Storage in Deep Saline Aquifers, *Oil Gas Sci.*  
953 *Technol. – Rev. l’Institut Français du Pétrole*, 65(3), 503–517, doi:10.2516/ogst/2009049.
- 954 Rudnicki, J. W. (2002), Diffusive instabilities in dilating and compacting geomaterials, in  
955 *Multiscale Deformation and Fracture in Materials and Structures, Solid Mechanics and Its*  
956 *Applications, Volume 84*, Kluwer Academic Publishers.
- 957 Rudnicki, J. W., and J. R. Rice (1975), Conditions for the localization of deformation in pressure-  
958 sensitive dilatant materials, *J. Mech. Phys. Solids*, 23(6), 371–394, doi:10.1016/0022-  
959 5096(75)90001-0.
- 960 Rustichelli, A., E. Tondi, F. Agosta, A. Cilona, and M. Giorgioni (2012), Development and  
961 distribution of bed-parallel compaction bands and pressure solution seams in carbonates  
962 (Bolognana Formation, Majella Mountain, Italy), *J. Struct. Geol.*, 37, 181–199,  
963 doi:10.1016/j.jsg.2012.01.007.
- 964 Rutqvist, J. (2012), The Geomechanics of CO<sub>2</sub> Storage in Deep Sedimentary Formations,  
965 *Geotech. Geol. Eng.*, 30(3), 525–551, doi:10.1007/s10706-011-9491-0.
- 966 Rutter, E. H. (1983), Pressure solution in nature, theory and experiment, *J. Geol. Soc. London.*,  
967 140(5), 725–740, doi:10.1144/gsjgs.140.5.0725.
- 968 Shin, H. (2009), Development of discontinuities in granular media, Georgia Institute of  
969 Technology.
- 970 Shin, H., and J. C. Santamarina (2009), Mineral Dissolution and the Evolution of  $k_0$ , *J. Geotech.*  
971 *Geoenvironmental Eng.*, 135(8), 1141–1147, doi:10.1061/(ASCE)GT.1943-5606.0000053.
- 972 Stefanou, I., and J. Sulem (2013), Chemical degradation and compaction instabilities in  
973 geomaterials, in *5th BIOT Conference on Poromechanics*, vol. 33, Vienne.

- 974 Sternlof, K. R., J. W. Rudnicki, and D. D. Pollard (2005), Anticrack inclusion model for  
975 compaction bands in sandstone, *J. Geophys. Res.*, *110*(B11), 1–16,  
976 doi:10.1029/2005JB003764.
- 977 Sulem, J., and H. Ouffroukh (2006), Shear banding in drained and undrained triaxial tests on a  
978 saturated sandstone: Porosity and permeability evolution, *Int. J. Rock Mech. Min. Sci.*,  
979 *43*(2), 292–310, doi:10.1016/j.ijrmms.2005.07.001.
- 980 Sulem, J., I. Stefanou, and E. Veveakis (2011), Stability analysis of undrained adiabatic shearing  
981 of a rock layer with Cosserat microstructure, *Granul. Matter*, *13*(3), 261–268,  
982 doi:10.1007/s10035-010-0244-1.
- 983 Tondi, E. (2007), Nucleation, development and petrophysical properties of faults in carbonate  
984 grainstones: Evidence from the San Vito Lo Capo peninsula (Sicily, Italy), *J. Struct. Geol.*,  
985 *29*(4), 614–628, doi:10.1016/j.jsg.2006.11.006.
- 986 Tondi, E., M. Antonellini, A. Aydin, L. Marchegiani, and G. Cello (2006), The role of  
987 deformation bands, stylolites and sheared stylolites in fault development in carbonate  
988 grainstones of Majella Mountain, Italy, *J. Struct. Geol.*, *28*(3), 376–391,  
989 doi:10.1016/j.jsg.2005.12.001.
- 990 Tran, M. K., H. Shin, Y.-H. Byun, and J.-S. Lee (2012), Mineral dissolution effects on  
991 mechanical strength, *Eng. Geol.*, *125*, 26–34, doi:10.1016/j.enggeo.2011.10.014.
- 992 Vardoulakis, I., and J. Sulem (1995), *Bifurcation Analysis in Geomechanics*, Blackie, Glasgow.
- 993 Veveakis, E., J. Sulem, and I. Stefanou (2012), Modeling of fault gouges with Cosserat  
994 Continuum Mechanics: Influence of thermal pressurization and chemical decomposition as  
995 coseismic weakening mechanisms, *J. Struct. Geol.*, *38*, 254–264,  
996 doi:10.1016/j.jsg.2011.09.012.
- 997 Veveakis, M., I. Stefanou, and J. Sulem (2013), Failure in shear bands for granular materials:  
998 thermo-hydro-chemo-mechanical effects, *Géotechnique Lett.*, *3*(April-June), 31–36,  
999 doi:10.1680/geolett.12.00063.
- 1000 Walsh, J. B., and W. F. Brace (1984), The effect of pressure on porosity and the transport  
1001 properties of rock, *J. Geophys. Res.*, *89*(B11), 9425, doi:10.1029/JB089iB11p09425.
- 1002 Wang, B., Y. Chen, and T. Wong (2008), A discrete element model for the development of  
1003 compaction localization in granular rock, *J. Geophys. Res.*, *113*(B3), B03202,  
1004 doi:10.1029/2006JB004501.
- 1005 Wong, T., and P. Baud (2012), The brittle-ductile transition in porous rock: A review, *J. Struct.*  
1006 *Geol.*, *44*, 25–53, doi:10.1016/j.jsg.2012.07.010.



- 1007 Xie, S. Y., J. F. Shao, and W. Y. Xu (2011), Influences of chemical degradation on mechanical  
1008 behaviour of a limestone, *Int. J. Rock Mech. Min. Sci.*, 48(5), 741–747,  
1009 doi:10.1016/j.ijrmms.2011.04.015.
- 1010 Zhu, W., P. Baud, and T. Wong (2010), Micromechanics of cataclastic pore collapse in  
1011 limestone, *J. Geophys. Res.*, 115(B4), B04405, doi:10.1029/2009JB006610.
- 1012 Zinsmeister, L., J. Dautriat, A. Dimanov, J. Raphanel, and M. Bornert (2013), Mechanical  
1013 evolution of an altered limestone using 2D and 3D digital image correlation (DIC), in *47th*  
1014 *U.S. Rock Mechanics / Geomechanics Symposium*, San Francisco, CA, USA.
- 1015
- 1016
- 1017

1018 **List of Captions**

1019	Figure 1. Positive feedback process due to dissolution and solid skeleton damage (e.g.	
1020	intergranular fracturing, breakage of the porous network, matrix cracking, grain-matrix	
1021	debonding etc.).....	6
1022	Figure 2. Schematic representation of the REV (macro-scale) and of the grains (micro-scale). The	
1023	picture is an idealization of the microstructure of a rock. The dissolution rate is homogeneous in	
1024	the REV when the size and the chemical composition of the grains is homogeneous. In the case	
1025	of compaction bands, the grains break, their size is not necessarily uniform in the REV and	
1026	consequently the dissolution rate is not any more homogeneous. ....	7
1027	Figure 3. Chemical isotropic softening due to dissolution of a constituent. $\zeta$ describes the ratio	
1028	of the residual mass of the constituent in the REV over its initial (reference) mass before the	
1029	dissolution process. Compression is taken negative. $\beta > 0$ corresponds to dilatancy and $\beta < 0$ to	
1030	contractancy (decrease of porosity).....	9
1031	Figure 4. Modified Cam-clay model with chemical softening. Compression negative. CSL stands	
1032	for the critical state line, which is assumed constant. ....	24
1033	Figure 5. Tendency for compaction bands for $n = 0.25$ . The more crushable the grains are, i.e. $a$	
1034	small, the bigger the coefficient $\Xi$ and the larger the region of instability is in $q - p$ plane. ....	25
1035	Figure 6. Tendency for compaction bands for $a = 0.1$ . The more porous the geomaterial is, the	
1036	bigger the coefficient $\Xi$ and the larger the region of instability in $q - p$ plane are.....	26
1037	Figure 7. Instability region (shaded) for compaction bands under oedometric conditions for	
1038	$a = 10^{-3}$ ( $\Xi = 200$ ). The points (in blue) represent the Issen & Rudnicki criterion for compaction	
1039	band instabilities. Different yield surfaces are drawn for different levels of chemical degradation	
1040	$\zeta$ .....	26
1041	Figure 8. Instability region (shaded) for compaction bands under oedometric conditions for	
1042	$a = 10^{-2}$ ( $\Xi = 20$ ). The points (in blue) represent the Issen & Rudnincky criterion for	
1043	compaction band instabilities. Different yield surfaces are drawn for different levels of chemical	
1044	degradation $\zeta$ .....	27
1045	Figure 9. Instability region (shaded) for compaction bands under oedometric conditions for $a = 1$	
1046	( $\Xi = 2$ ). The points (in blue) represent the Issen & Rudnincky criterion for compaction bands.	
1047	Different yield surfaces are drawn for different levels of chemical degradation $\zeta$ .....	27

1048	Figure 10. Instability growth coefficient $s$ in terms of the perturbation wavelength $\lambda$ for $\ell_c = 0$ .	
1049	The growth coefficient is positive and the system is unstable. ....	28
1050	Figure 11. Growth coefficient, $s$ , in terms of the perturbation wave length for $a = 10^{-2}$ and	
1051	$\ell_c \approx 4$ . The dominant wave length corresponds to the value of $\lambda$ for which the growth	
1052	coefficient is maximum. The thickness of the compaction band is proportional to the dominant	
1053	wave length. ....	31
1054	Figure 12. Influence of hydraulic diffusivity on the dominant wavelength for $a = 10^{-2}$ and $\ell_c \approx 4$ .	
1055	The red dots represent the maximum value of the Lyapunov exponent for a given hydraulic	
1056	diffusivity. The more impermeable the medium is the more localized the compaction instability	
1057	becomes (smaller wavelength). ....	32
1058	Figure 13. Dominant wave length (wave length selection) in terms of the grain damage	
1059	parameter $a$ . As the grains become less crushable, $\lambda_{\max}$ tends to infinity and therefore the	
1060	formation of compaction bands is less likely. ....	33
1061	Figure 14. Dominant wave length (wave length selection) in terms of the grain damage parameter	
1062	$a$ for various values of the dissolution rate ( $k^*$ in m/s). The faster the reaction is the narrower	
1063	the compaction band zone is. ....	33
1064	Figure 15. Instability region (shaded) for compaction bands under oedometric conditions for a	
1065	sandstone at 4 km depth. Different yield surfaces are drawn for different levels of chemical	
1066	degradation, $\zeta$ . The stress path 1 represents the elastic loading of the material under oedometric	
1067	conditions, while the stress path 2 represents the path that the material follows after yielding. ...	36
1068	Figure 16. Instability region (shaded) for compaction bands under oedometric conditions for a	
1069	carbonate grainstone at 1.8 km depth. Different yield surfaces are drawn for different levels of	
1070	chemical degradation, $\zeta$ . The stress path line no. 1 represents the elastic loading of the material	
1071	under oedometric conditions, while the stress path line no. 2 represents the path that the material	
1072	follows after yielding. ....	39
1073		